Robust gain-scheduled autopilot design with anti-windup compensation for a guided projectile

Thai, Sovanna; Theodoulis, Spilios; Roos, Clément; Biannic, Jean Marc

DOI
10.1007/s13272-023-00668-9

Publication date
2023

Document Version
Final published version

Published in
CEAS Aeronautical Journal

CEAS Aeronautical Journal
https://doi.org/10.1007/s13272-023-00668-9

ORIGINAL PAPER

Robust gain-scheduled autopilot design with anti-windup compensation for a guided projectile

Sovanna Thai[1,3] · Spilios Theodoulis[1,4] · Clément Roos[2] · Jean-Marc Biannic[2]

Received: 9 November 2022 / Revised: 16 May 2023 / Accepted: 22 May 2023

Abstract
This article deals with the control design of a dual-spin projectile concept, characterized by highly nonlinear parameter-dependent and coupled dynamics, and subject to uncertainties and actuator saturations. An open-loop nonlinear model stemming from flight mechanics is first developed. It is subsequently linearized and decomposed into a linear parameter-varying system for the roll channel, and a quasi-linear parameter-varying system for the pitch/yaw channels. The obtained models are then used to design gain-scheduled $\mathcal{H}_\infty$ baseline autopilots, which do not take the saturations into account. As a major contribution of this paper, the saturation nonlinearities are addressed in a second step through anti-windup augmentation. Three anti-windup schemes are proposed, which are evaluated and compared through time-domain simulations and integral quadratic constraints analysis. Finally, complete guided flight scenarios involving a wind disturbance, perturbed launch conditions, or aerodynamic uncertainties, are analyzed by means of nonlinear Monte Carlo simulations to evaluate the improvements brought by the proposed anti-windup compensators.

Keywords Guided projectiles · Anti-windup · Gain scheduling · Robustness analysis

1 Introduction

Standard ballistic projectiles suffer from a lack of accuracy, due to various factors such as incorrect launch conditions or wind perturbations. As a consequence, multiple rounds must typically be fired to intercept a single target. This leads to significant risks of collateral damage, high deployment and operational costs, and logistical concerns. Guided projectiles aim to overcome these limitations. Among the numerous guided projectile concepts, that of a course correction fuse (CCF) decoupled from the body and equipped with canards has numerous advantages over other steering mechanisms proposed in the literature on guided projectiles. Unlike impulse jet thrusters [1–3] or inertial loads [4–6], aerodynamic surfaces provide a correction which can be modeled in continuous time as aerodynamic effects. Additional benefits of the dual-spin configuration, as opposed to fin-stabilized projectiles, are the capability to retrofit existing unguided shells, thus greatly reducing development costs, and a greater range due to the lack of stabilizing surfaces [7]. This solution leads to a guided projectile with seven degrees of freedom (7-DoF), whose precision and performance are then highly dependent on the embedded hardware and flight control algorithms. In turn, the development of flight control algorithms relies on a mathematical model of the system to control. This model must be a sufficiently accurate description of the behavior of the system, while also being compatible with control design methods.

Literature on control theory applied to guided projectiles remains scarce relative to other aerospace systems, such as aircraft, space launchers, and UAVs. Several ad hoc

✉ Sovanna Thai
sovanna.thai@airbus.com

Spilios Theodoulis
s.theodoulis@tudelft.nl

Clément Roos
clement.roos@onera.fr

Jean-Marc Biannic
jean-marc.biannic@onera.fr

[1] French-German Research Institute of Saint-Louis, 5 Rue du Général Cassagnou, 68300 Saint-Louis, France

[2] ONERA The French Aerospace Lab, 2 Avenue Edouard Belin, 31400 Toulouse, France

[3] Present Address: Airbus Defence and Space, 31 Rue des Cosmonautes, 31400 Toulouse, France

[4] Present Address: Delft University of Technology, Kluyverweg 1, 2629 HS Delft, The Netherlands

Published online: 05 July 2023

open-loop algorithms based on trajectory tracking or impact point prediction [8] have been investigated for a wealth of steering mechanisms, but these approaches fail to handle aerodynamic uncertainties in a satisfying manner. Regarding the dual-spin configuration, the first full nonlinear model was published in [9] for an unguided projectile, while early results on the control of such systems based on trajectory tracking can be found in [10, 11]. Recent studies [12–14] developed linearization algorithms specific to dual-spin projectiles, as well as efficient autopilots based on gain-scheduling techniques [15, 16] and on local $\mathcal{H}_\infty$ syntheses [17, chap. 9] for canards acting in pairs, demonstrating that the control of such nonlinear systems can be addressed using the more familiar methods from linear control theory. In line with these developments, this paper, resulting from a PhD work [18], extends the proposed linear framework by addressing canard saturations using techniques from modern anti-windup design theory [19], as well as integral quadratic constraints (IQC) analysis [20] to evaluate the local robustness properties of the augmented closed-loop systems.

This paper is organized as follows. Section 2 sets up the model of the projectile airframe that will be used to tackle the control problems: compared to [14], the present study uses a slightly different steering mechanism where all three axes of the projectile are aerodynamically controlled using the canards, removing the need for a coaxial motor within the fuse. The obtained models are then used in Sect. 3 to design a baseline autopilot, which does not take saturations into account. The saturation nonlinearities are addressed in Sect. 4 through anti-windup design. In Sect. 5, complete guided flight scenarios involving a wind disturbance, perturbed launch conditions or aerodynamic uncertainties are simulated to evaluate the various anti-windup schemes.

2 Open-loop modeling

2.1 Presentation of the guided projectile concept

The guided projectile concept studied in this paper is a dual-spin projectile consisting of a standard 155 mm ammunition retrofitted with a roll-decoupled fuse. The body, or aft part, contains the explosive payload. The fuse, or forward part, is equipped with four canards, as shown in Fig. 1, which are independently actuated. The CCF concept considered here differs from [14], where a coaxial motor dedicated to roll control is included. Instead, all three axes are aerodynamically controlled using the canards.

The flight scenario of the studied projectile can be broken into several phases, depicted in Fig. 2. At the start of the ballistic phase ($0 \leq t < t_{\text{start}} = 20$ s), electronic components are switched on. This is done a few seconds after launch

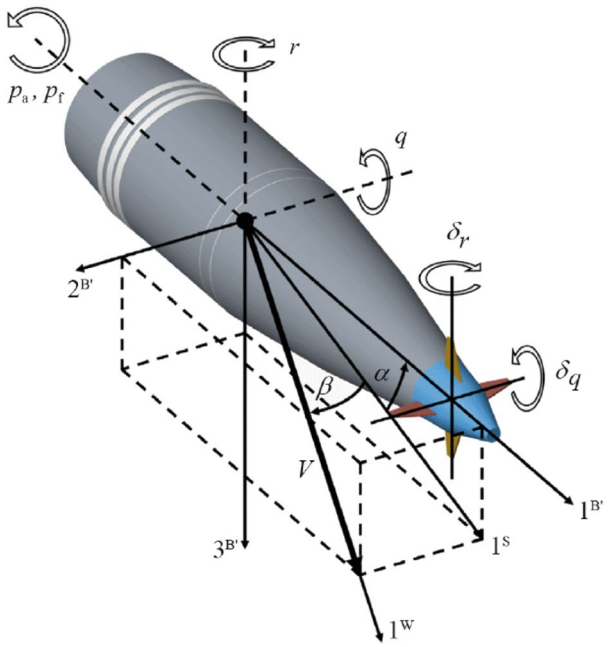

Fig. 1 155 mm projectile with a course correction fuse equipped with canards

to avoid possible hardware degradations due to the harsh initial conditions. At $t = t_{\text{start}}$, the fuse roll rate p_f, which at this point is high due to the mechanical bearing between the body and the fuse, is decreased by maintaining constant deflection angles until the moment t_{switch} when the roll rate reaches $p_f = 1800$ deg/s $= 10\pi$ rad/s. The roll autopilot is then activated to stabilize the fuse at a fixed roll angle ϕ_f. Finally, the projectile enters its guided phase at $t_{\text{guid}} = 30$ s, during which additional efforts on the pitch and yaw axes are generated by the canards to alter its trajectory.

2.2 Nonlinear modeling using flight mechanics

The 7-DoF airframe model is described by its translational and attitude dynamic equations, given, respectively, by Newton's and Euler's laws of motions. These are expressed in a non-rolling frame as:

$$\begin{bmatrix} \dot{u} \\ \dot{v} \\ \dot{w} \end{bmatrix} = \frac{1}{m}\begin{bmatrix} X \\ Y \\ Z \end{bmatrix} - \begin{bmatrix} 0 & -r & q \\ r & 0 & r\tan\theta \\ -q & -r\tan\theta & 0 \end{bmatrix}\begin{bmatrix} u \\ v \\ w \end{bmatrix} \tag{1}$$

$$\begin{bmatrix} \dot{p}_f \\ \dot{p}_a \\ \dot{q} \\ \dot{r} \end{bmatrix} = \begin{bmatrix} L_f/I_{xf} \\ L_a/I_{xa} \\ M/I_t \\ N/I_t \end{bmatrix} + \begin{bmatrix} 0 \\ 0 \\ -\left(I_{xa}I_t^{-1}p_a + r\tan\theta\right)r \\ \left(I_{xa}I_t^{-1}p_a + r\tan\theta\right)q \end{bmatrix} \tag{2}$$

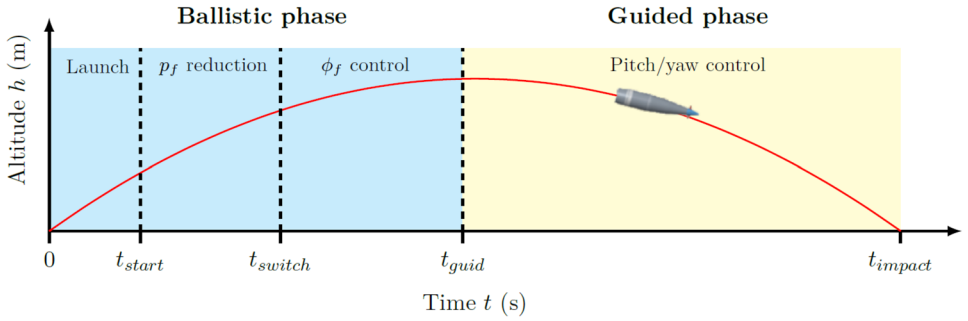

Fig. 2 Standard flight scenario of a canard-guided dual-spin projectile

where $[u\ v\ w]^{\mathrm{T}}$ are the linear velocities, and $[p_f\ p_a\ q\ r]^{\mathrm{T}}$ are the angular rates (the subscripts f and a denote the forward and aft parts, respectively). The constants appearing in these equations are the mass m of the projectile, the longitudinal moments of inertia of the front and aft part I_{xf}, I_{xa}, and the transversal moment of inertia I_t. Complementing these equations are the translational and attitude kinematic equations, which describe the linear and angular positions $[x_e\ y_e\ z_e]^{\mathrm{T}}$ and $[\phi_f\ \phi_a\ \theta\ \psi]^{\mathrm{T}}$ with respect to the inertial Earth frame [21, chap. 3]:

$$\begin{bmatrix}\dot{x}_e\\ \dot{y}_e\\ \dot{z}_e\end{bmatrix}=\begin{bmatrix}\cos\psi\cos\theta & -\sin\psi & \cos\psi\sin\theta\\ \sin\psi\cos\theta & \cos\psi & \sin\psi\sin\theta\\ -\sin\theta & 0 & \cos\theta\end{bmatrix}\begin{bmatrix}u\\ v\\ w\end{bmatrix} \tag{3}$$

$$\begin{bmatrix}\dot{\phi}_f\\ \dot{\phi}_a\\ \dot{\theta}\\ \dot{\psi}\end{bmatrix}=\begin{bmatrix}1&0&0&\tan\theta\\ 0&1&0&\tan\theta\\ 0&0&1&0\\ 0&0&0&1/\cos\theta\end{bmatrix}\begin{bmatrix}p_f\\ p_a\\ q\\ r\end{bmatrix} \tag{4}$$

The most important efforts applied on the projectile are aerodynamic in nature. For this reason, aerodynamic variables are more useful than the linear velocities, both as state variables and to describe the forces and moments. Hence, assuming no wind, we define the airspeed V, angle of attack (AoA) α, and angle of sideslip (AoS) β as:

$$V=\sqrt{u^2+v^2+w^2},\quad \alpha=\arctan\left(\frac{w}{u}\right),\quad \beta=\arctan\left(\frac{v}{\sqrt{u^2+w^2}}\right) \tag{5}$$

Differentiation of the above variables allow to rewrite Eq. (1) in a form that is more suitable for control design purposes:

$$\begin{bmatrix}\dot{V}\\ \dot{\alpha}\\ \dot{\beta}\end{bmatrix}=\begin{bmatrix}0\\ q+r(\cos\alpha\tan\theta-\sin\alpha)\tan\beta\\ -r(\cos\alpha+\sin\alpha\tan\theta)\end{bmatrix}+\frac{1}{mV}\begin{bmatrix}V\cos\alpha\cos\beta & V\sin\beta & V\sin\alpha\cos\beta\\ -\sin\alpha/\cos\beta & 0 & \cos\alpha/\cos\beta\\ -\cos\alpha\sin\beta & \cos\beta & -\sin\alpha\sin\beta\end{bmatrix}\begin{bmatrix}X\\ Y\\ Z\end{bmatrix} \tag{6}$$

The modeling of the forces $[X\ Y\ Z]^{\mathrm{T}}$ and moments $[L_f\ L_a\ M\ N]^{\mathrm{T}}$ is based on aeroballistics theory as presented in [22, chap. 2]. The external forces include body, Magnus (originating from the spinning motion), control (generated by the canards), and gravitational terms:

$$\begin{bmatrix}X\\ Y\\ Z\end{bmatrix}=\bar{q}S\left(\begin{bmatrix}-C_A(\mathcal{M},\alpha')\\ -C_{N\alpha}(\mathcal{M},\alpha')\beta\\ -C_{N\alpha}(\mathcal{M},\alpha')\alpha\end{bmatrix}+\frac{p_a d}{2V}\begin{bmatrix}0\\ C_{Yp\alpha}(\mathcal{M})\alpha\\ -C_{Yp\alpha}(\mathcal{M})\beta\end{bmatrix}+\begin{bmatrix}0\\ -C_{N\delta}(\mathcal{M})\delta_r\\ -C_{N\delta}(\mathcal{M})\delta_q\end{bmatrix}\right)+mg\begin{bmatrix}-\sin\theta\\ 0\\ \cos\theta\end{bmatrix} \tag{7}$$

The external moments consist of body pitching, Magnus, damping, control, and friction terms:

$$\begin{bmatrix}L_f\\ L_a\\ M\\ N\end{bmatrix}=\bar{q}Sd\left(\begin{bmatrix}0\\ 0\\ C_{m\alpha}(\mathcal{M},\alpha')\alpha\\ -C_{m\alpha}(\mathcal{M},\alpha')\beta\end{bmatrix}+\frac{p_a d}{2V}\begin{bmatrix}0\\ 0\\ C_{np\alpha}(\mathcal{M})\beta\\ C_{np\alpha}(\mathcal{M})\alpha\end{bmatrix}+\frac{d}{2V}\begin{bmatrix}0\\ C_{lp}(\mathcal{M})p_a\\ C_{mq}(\mathcal{M})q\\ C_{mq}(\mathcal{M})r\end{bmatrix}+\begin{bmatrix}0\\ -C_{l\delta}(\mathcal{M})\delta_p\\ C_{m\delta}(\mathcal{M})\delta_q\\ -C_{m\delta}(\mathcal{M})\delta_r\end{bmatrix}\right)+\begin{bmatrix}L_{f-a}\\ -L_{f-a}\\ 0\\ 0\end{bmatrix} \tag{8}$$

The expressions of the forces and moments involve aerodynamic coefficients that depend in a nonlinear manner on the Mach number $\mathcal{M}=V/a(h)$, with a the altitude-dependent speed of sound, and for some also on the angle of incidence (AoI) α':

$$\alpha'=\arccos\left(\frac{u}{V}\right)=\arccos(\cos\alpha\cos\beta) \tag{9}$$

Due to limitations on wind-tunnel measurements, these aerodynamic coefficients take uncertain values around their nominal values. The considered uncertainty levels are reported in Table 1.

Table 1 Aerodynamic coefficient uncertainties

Force coefficient	Uncertainty (%)	Moment coefficient	Uncertainty (%)
C_A	3	–	–
$C_{N\alpha}$	6	$C_{m\alpha}$	3
$C_{Yp\alpha}$	33	$C_{np\alpha}$	25
–	–	C_{lp}	15
–	–	C_{mq}	15
$C_{N\delta}$	15	$C_{l\delta}$	15
–	–	$C_{m\delta}$	15

Other parameters and constants appearing in the expressions of the forces and moments are the dynamic pressure $\overline{q} = \frac{1}{2}\rho(h)V^2$, with $\rho(h)$ the air density, the gravitational acceleration g, the reference area S, and the caliber d. The control variables $[\delta_p\ \delta_q\ \delta_r]^{\mathrm{T}}$ are virtual control signals depending on the roll angle of the fuse ϕ_f and the real canard deflection angles $[\delta_1\ \delta_2\ \delta_3\ \delta_4]^{\mathrm{T}}$ through the relation [23, chap. 3]:

$$\begin{bmatrix}\delta_p\\ \delta_q\\ \delta_r\end{bmatrix} = T_{VR}(\phi_f)\begin{bmatrix}\delta_1\\ \delta_2\\ \delta_3\\ \delta_4\end{bmatrix} = \begin{bmatrix}1 & 0 & 0\\ 0 & \cos\phi_f & -\sin\phi_f\\ 0 & \sin\phi_f & \cos\phi_f\end{bmatrix} \begin{bmatrix}\frac{1}{4} & \frac{1}{4} & \frac{1}{4} & \frac{1}{4}\\ 0 & \frac{1}{2} & 0 & -\frac{1}{2}\\ \frac{1}{2} & 0 & -\frac{1}{2} & 0\end{bmatrix}\begin{bmatrix}\delta_1\\ \delta_2\\ \delta_3\\ \delta_4\end{bmatrix} \tag{10}$$

Finally, the friction moment L_{f-a} between the forward and aft part is given by:

$$L_{f-a} = \overline{q}SC_A(\mathcal{M},\alpha,\beta)\,\mathrm{sign}\left(p_a - p_f\right)\left(K_s + K_v|p_a - p_f|\right) \tag{11}$$

with K_s and K_v static and viscous friction coefficients with an uncertainty level of 40%.

2.3 Linearized models for the roll and pitch/yaw channels

The nonlinear model of the airframe can be decomposed into the roll channel on one hand, and the pitch/yaw channels on the other hand. This decomposition corresponds to the two separate control problems broached in Sect. 2.1.

2.3.1 LPV model of the roll channel

The states of interest for the control of the roll channel are the roll angle ϕ_f of the fuse and its angular rate p_f. Their dynamics can be extracted from Eqs. (1) and (3) and rewritten in the following LPV form:

$$\begin{bmatrix}\dot{\phi}_f\\ \dot{p}_f\end{bmatrix} = \begin{bmatrix}0 & 1\\ 0 & a_{22}(\boldsymbol{\sigma}_R)\end{bmatrix}\begin{bmatrix}\phi_f\\ p_f\end{bmatrix} + \begin{bmatrix}0\\ b_2(\boldsymbol{\sigma}_R)\end{bmatrix}\delta_p + \begin{bmatrix}d_\phi\\ d_p\end{bmatrix} \tag{12}$$

where:

$$a_{22}(\boldsymbol{\sigma}_R) = -\left(\frac{\overline{q}Sd}{I_{xf}}\right)C_A(\mathcal{M},\alpha')K_v$$
$$b_2(\boldsymbol{\sigma}_R) = -\left(\frac{\overline{q}Sd}{I_{xf}}\right)C_{l\delta}(\mathcal{M}) \tag{13}$$

and $\boldsymbol{\sigma}_R = \left[\alpha'\ V\ h\right]^{\mathrm{T}}$ is a parameter vector. The time-varying disturbance terms d_ϕ and d_p are given by:

$$d_\phi = r\tan\theta \qquad d_p = \left(\frac{\overline{q}Sd}{I_{xf}}\right)$$
$$C_A(\mathcal{M},\alpha')[\,\mathrm{sign}\left(p_a - p_f\right)K_s + K_v p_a] \tag{14}$$

Ballistic simulations show that in practical flight conditions, $\alpha' \in [0\ \mathrm{deg}, 15\ \mathrm{deg}]$, and the value of the drag coefficient $C_A(\mathcal{M},\alpha')$ is predominantly governed by the value of the Mach number, i.e., by the parameters V and h. This observation leads to considering a reduced parameter vector $\boldsymbol{\lambda}_R = [V\ h]^{\mathrm{T}}$ of scheduling variables.

2.3.2 Linearized model for the pitch/yaw channels

The relevant nonlinear dynamics for the pitch/yaw channels can be rewritten in the generic parameter-dependent form:

$$\begin{cases}\dot{\boldsymbol{x}} = f(\boldsymbol{x},\boldsymbol{u},\boldsymbol{\sigma}_{PY})\\ \boldsymbol{y} = g(\boldsymbol{x},\boldsymbol{u},\boldsymbol{\sigma}_{PY})\end{cases} \tag{15}$$

with states $\boldsymbol{x} = \left[\alpha\ q\ \beta\ r\right]^{\mathrm{T}}$, inputs $\boldsymbol{u} = \left[\delta_q\ \delta_r\right]^{\mathrm{T}}$, outputs $\boldsymbol{y} = \left[n_z\ n_y\ q\ r\right]^{\mathrm{T}}$, and parameters $\boldsymbol{\sigma}_{PY} = \left[V\ h\ p_a\ \theta\right]^{\mathrm{T}}$. The outputs n_z and n_y are the normal and lateral load factors, respectively, defined as the contribution of the external forces excluding gravity, divided by the projectile weight mg, and expressed in g.

In view of designing a gain-scheduled controller, a Jacobian linearization around trim points is performed on the nonlinear model [15, 16]. The procedure starts with the computation of trim points for fixed values $\overline{\boldsymbol{\sigma}}_{PY} = [\overline{V}\ \overline{h}\ \overline{p_a}\ \overline{\theta}]^{\mathrm{T}}$ of the parameter vector. That is, we seek the solutions $(\overline{\boldsymbol{x}},\overline{\boldsymbol{u}})$ of the equation:

$$f\left(\overline{\boldsymbol{x}},\overline{\boldsymbol{u}},\overline{\boldsymbol{\sigma}}_{PY}\right) = 0 \tag{16}$$

However, the above system is underdetermined, since it consists of four equations with six unknown variables. To overcome this issue, we define an extended trimming vector $\overline{\boldsymbol{\rho}} = [\overline{V}\ \overline{h}\ \overline{p_a}\ \overline{\theta}\ \overline{\alpha}\ \overline{\beta}]^{\mathrm{T}}$ by also imposing the values of

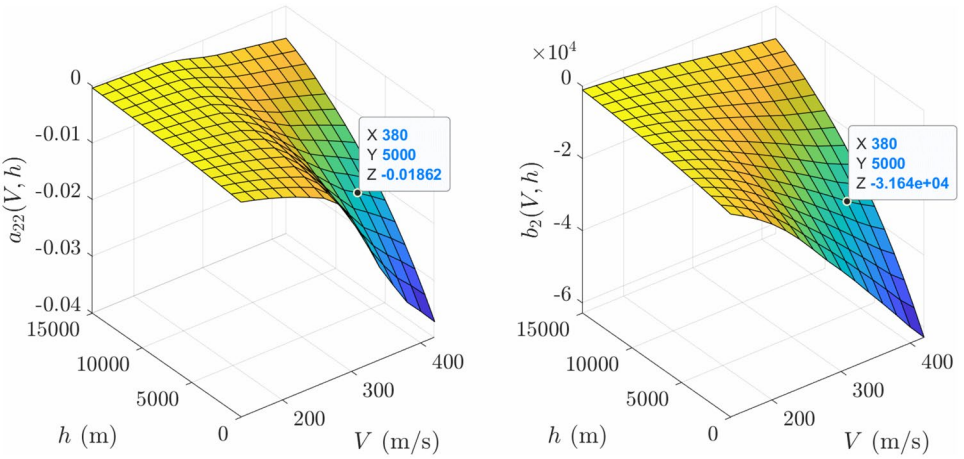

Fig. 3 Variation of the state-space coefficients over the flight envelope and chosen design point λ_{R0}

the AoA and AoS. The solutions $(\overline{\boldsymbol{x}}, \overline{\boldsymbol{u}})$ can then be analytically computed, and are also exploited to compute the corresponding equilibrium outputs $\overline{\boldsymbol{y}}$ (see [24] for details on the resolution). Defining the deviation variables $\boldsymbol{x}_\varepsilon = \boldsymbol{x} - \overline{\boldsymbol{x}}$, $\boldsymbol{u}_\varepsilon = \boldsymbol{u} - \overline{\boldsymbol{u}}$, and $\boldsymbol{y}_\varepsilon = \boldsymbol{y} - \overline{\boldsymbol{y}}$, the nonlinear dynamics can then be approximated by a first-order Taylor expansion and written in state-space form:

$$\begin{cases} \dot{\boldsymbol{x}}_\varepsilon = \boldsymbol{A}(\overline{\boldsymbol{\rho}})\boldsymbol{x}_\varepsilon + \boldsymbol{B}(\overline{\boldsymbol{\rho}})\boldsymbol{u}_\varepsilon \\ \boldsymbol{y}_\varepsilon = \boldsymbol{C}(\overline{\boldsymbol{\rho}})\tilde{\boldsymbol{x}}_\varepsilon + \boldsymbol{D}(\overline{\boldsymbol{\rho}})\boldsymbol{u}_\varepsilon \end{cases} \tag{17}$$

Since the trimming vector used to compute equilibrium points contains state variables, and using a common abuse of language, the bank of LTI models described by Eq. (17) and parametrized by $\boldsymbol{\rho}$ is referred to as a quasi-LPV model. To reduce the computational burden of the controller synthesis step, only the most influential parameters are kept as scheduling variables. Exploiting the simulation-based sensitivity analysis done in [14], the reduced trim vector $\lambda_{PY} = [V\ h\ p_a]^{\mathrm{T}}$ is considered. The three-dimensional flight envelope is described by the intervals $V \in [140\ \text{m/s}, 380\ \text{m/s}]$, $h \in [0\ \text{m}, 15000\ \text{m}]$, and $p_a \in [750\ \text{rad/s}, 1650\ \text{rad/s}]$, with the remaining parameters fixed to: $\theta = -17.5\ \text{deg}$, $\alpha = 0\ \text{deg}$, and $\beta = 0\ \text{deg}$.

2.4 Definition of the actuator and sensor models

The four servomotors actuating the canards are modeled as identical second-order systems with natural frequency $\omega_{\text{act}} = 2\pi \times 20\ \text{rad/s}$ and damping ratio $\xi_{\text{act}} = 0.781$. In addition, a position saturation $\delta_{\text{sat}} = \pm 10\ \text{deg}$ is introduced at the input of each actuator. This saturation level does not come from mechanical limitations, but rather from considerations regarding the validity of the aerodynamic model, and specifically the expressions of the canard forces and moments which rely on a small angle assumption. The actuator output signals are converted into the virtual control signals using Eq. (10).

Since the roll and pitch/yaw control problems are treated separately, it is natural to consider the roll autopilot output as a commanded value $\delta_{p,c}$ on the virtual signal δ_p, and the pitch/yaw autopilot outputs as commanded values $(\delta_{q,c}, \delta_{r,c})$ on (δ_q, δ_r). The commanded virtual signals must then be allocated to the four actuators. A natural choice for the allocation matrix is to use the pseudo-inverse $T_{\text{VR}}(\phi_f)^{\dagger}$.

The fuse is equipped with accelerometers providing load factor measurements $(n_{z,m}, n_{y,m})$, and with gyroscopes providing measurements $(p_{f,m}, q_m, r_m)$ of the angular rates. In addition, sensors from the servomotors give measurements $(\delta_{1,m}, \delta_{2,m}, \delta_{3,m}, \delta_{4,m})$ of the canard deflection angles. Equation (10) can then be used again to obtain measurements $(\delta_{p,m}, \delta_{q,m}, \delta_{r,m})$ of the virtual control signals. For simplicity, all sensors are given the same dynamics, described by a first-order model of natural frequency $\omega_s = 2\pi \times 133\ \text{rad/s}$.

Remark 1 The impact of the position of the sensors is not taken into account in this study. The signals $(n_{z,m}, n_{y,m})$ then correspond to the measured load factors at the projectile center of mass. A more representative model could be obtained by applying the Grubin transformation [21], as done in [13].

3 Baseline autopilot design

In this section, control design is tackled without taking saturations into account, leading to a so-called baseline autopilot. Importantly, we do not seek to fine-tune the controller for robust performance. Rather, the aim is limited to designing a baseline autopilot with high enough performance to

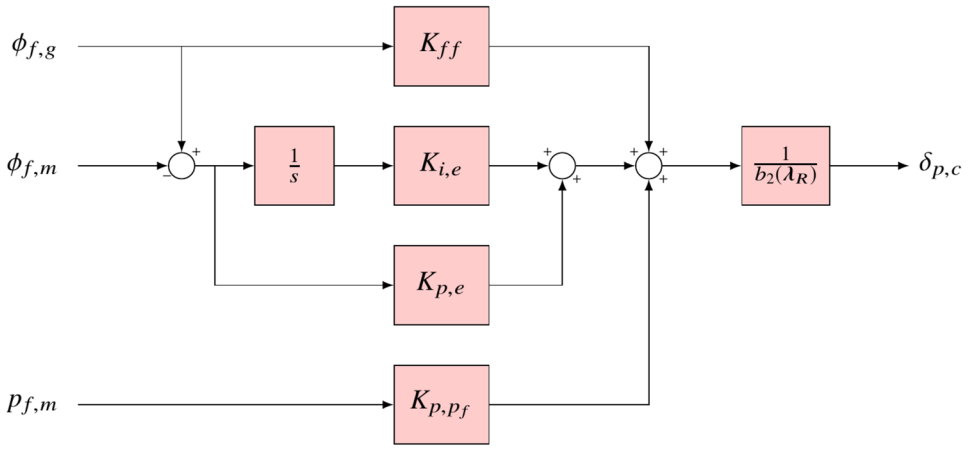

Fig. 4 Roll autopilot structure

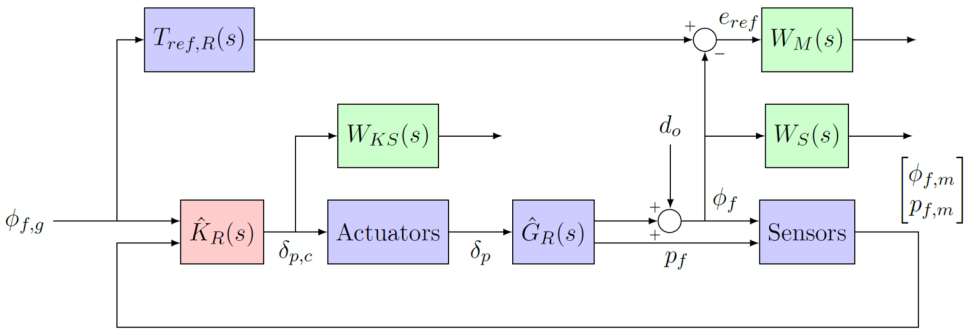

Fig. 5 Structured $\mathcal{H}_\infty$ synthesis problem for the roll autopilot

contemplate anti-windup augmentation, which is addressed in Sect. 4.

3.1 Roll autopilot design

3.1.1 Control objectives and strategy

To tackle the roll autopilot design problem, the LPV system of Eq. (12) describing the roll dynamics is simplified by considering the reduced parameter vector $\lambda_R = [V\ h]^{\mathrm{T}}$ instead of $\boldsymbol{\sigma}_R$, and by neglecting the disturbances $[d_\phi\ d_{p_f}]^{\mathrm{T}}$. This system has one pole at 0 and another pole given by $a_{22}(\lambda_R)$. The variations of $a_{22}(\lambda_R)$ and $b_2(\lambda_R)$ are shown in Fig. 3. Noticeably, the variations of the second pole are restricted to a small interval in the left-half plane. It is, therefore, reasonable to approximate this coefficient with a constant $\overline{a_{22}}$. The transfer function from δ_p to $\left[\phi_f\ p_f\right]^{\mathrm{T}}$ then takes the form:

$$G_R(s,\lambda_R) = b_2(\lambda_R)\begin{bmatrix} \dfrac{1}{s(s-\overline{a_{22}})} \\ \dfrac{1}{s-\overline{a_{22}}} \end{bmatrix} = b_2(\lambda_R)\hat{G}_R(s) \tag{18}$$

Thus, the chosen control strategy consists of designing a controller $\hat{K}_R(s)$ associated to the LTI system $\hat{G}_R(s)$. Then a gain-scheduled controller for $G_R(s, \lambda_R)$ is directly obtained as:

$$K_R(s,\lambda_R) = \frac{1}{b_2(\lambda_R)}\hat{K}_R(s) \tag{19}$$

Since only one design point is needed, this strategy drastically simplifies the design step, and the relevance of the approximations can be validated with *a posteriori* analyses and simulations. The design point $\lambda_{R0} = [V = 380\ \text{m/s},\ h = 5000\ \text{m}]^{\mathrm{T}}$ is chosen from a 15×16 grid of the reduced flight envelope so as to minimize the distance of $a_{22}(\lambda_{R0})$ to the midpoint $\frac{1}{2}\left(\max_{\lambda_R} a_{22}(\lambda_R) - \min_{\lambda_R} a_{22}(\lambda_R)\right)$.

3.1.2 Autopilot structure and tuning

The proposed fixed-structure controller is shown in Fig. 4. It consists of a PI-P controller (gains $K_{p,e}$, $K_{i,e}$, and K_{p,p_f}) with an additional feedforward gain K_{ff} to help with reference tracking. Recall that the subscripts g and m refer to guidance

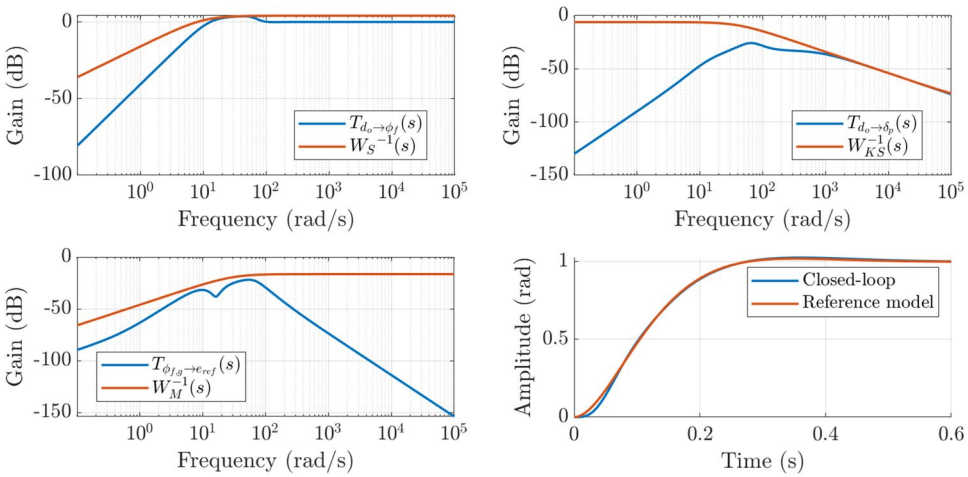

Fig. 6 Closed-loop transfer functions for disturbance rejection (upper left), control attenuation (upper right), model matching (lower left), and unit step response (lower right)

signals and sensor measurements, respectively. The controller gains are computed by solving a structured $\mathcal{H}_\infty$ synthesis problem [17, 25], illustrated by the block-diagram of Fig. 5. The closed-loop roll channel is augmented with weighting functions $W_S(s)$, $W_{KS}(s)$, and $W_M(s)$, corresponding, respectively, to low frequency disturbance rejection, high frequency control signal attenuation, and model matching in the low to intermediate frequencies. The reference model $T_{\text{ref},R}(s)$ used for the model matching requirement of the transfer from the guidance signal $\phi_{f,g}$ to the roll angle ϕ_f is given by a second-order system of frequency $\omega_{\text{ref},R} = 14.3$ rad/s and damping ratio $\xi_{\text{ref},R} = 0.781$. Since an accurate model matching is not perceived as an imperative for the roll autopilot design, the related requirement is given as a soft constraint. Thus, the optimization problem to solve is:

$$\begin{aligned} \underset{\boldsymbol{\kappa}_R}{\text{minimise}} \;& \|W_M(s)\mathcal{T}_{\phi_{f,g}\to e_{ref}}(s)\|_\infty \\ \text{subject to} \;& \|W_S(s)\mathcal{T}_{d_o\to\phi_f}(s)\|_\infty < 1 \\ & \|W_{KS}(s)\mathcal{T}_{d_o\to\delta_p}(s)\|_\infty < 1 \end{aligned} \tag{20}$$

where $\boldsymbol{\kappa}_R = \left[K_{i,e}\; K_{p,e}\; K_{p,p_f}\; K_{ff}\right]^{\mathrm{T}}$. The weighting functions are selected as follows:

$$\begin{aligned} W_M(s) &= \frac{s+30}{0.15s+30\times10^{-4}} \\ W_S(s) &= \frac{s+10}{1.6s+10\times10^{-4}} \\ W_{KS}(s) &= \frac{s+40}{10^{-4}s+40\times0.5} \end{aligned} \tag{21}$$

The optimization problem is solved using the `systune` routine of the Matlab Control System Toolbox, which yields a performance index (value of the soft constraint) of $\gamma = 0.62$. The resulting shaped transfer functions and closed-loop step response are shown in Fig. 6, illustrating the fulfillment of the specifications and very good model matching.

3.1.3 Robustness analysis and closed-loop time-domain simulations

Robustness with respect to uncertainties is assessed using μ-analysis [26], whose principles are briefly summarized here. As a preliminary step, the uncertain LTI system to analyze must be put in the form of a $(M(s), \Delta)$ interconnection as shown in Fig. 7, called a Linear Fractional Representation (LFR). The LTI system $M(s) = \begin{bmatrix} M_{11}(s) & M_{12}(s) \\ M_{21}(s) & M_{22}(s) \end{bmatrix}$ represents the nominal closed-loop system, and the operator Δ gathers all the uncertainties into a block-diagonal operator of the form:

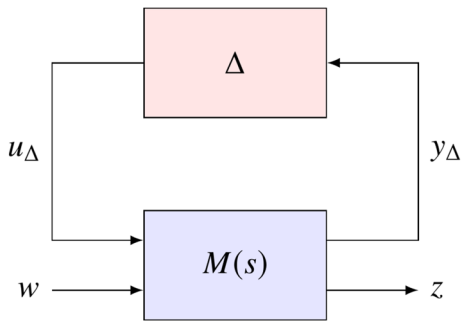

Fig. 7 LFR of a system with parametric uncertainties

$$\Delta = \text{diag}\,(\Delta_1, \ldots, \Delta_N) \tag{22}$$

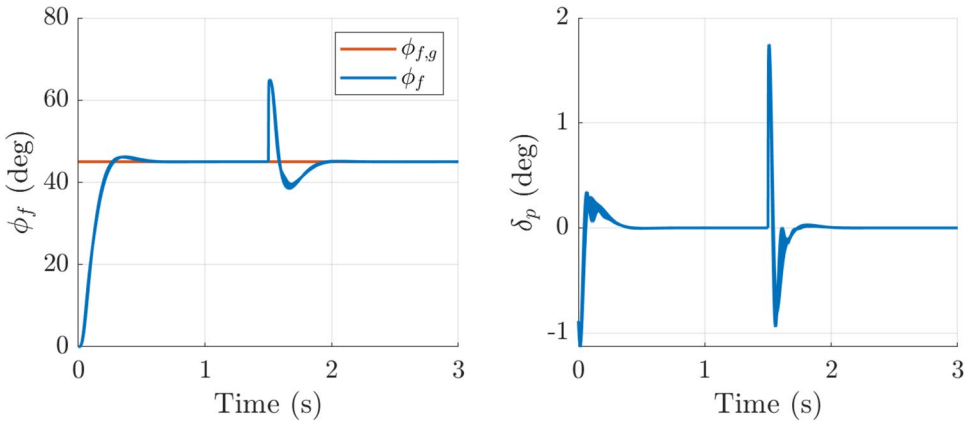

Fig. 8 Simulation at the design point with model uncertainties: roll angle (left), virtual roll control signal (right)

where each Δ_i is a time-invariant diagonal matrix $\Delta_i = \delta_i I_{n_i}$, with δ_i a real parametric uncertainty. The set of matrices with the block-diagonal structure described above is denoted $\mathbf{\Delta}$, and corresponds to the set of physically meaningful uncertainties. If all uncertainties are bounded, the LFR can be normalized so that physically meaningful uncertainties are restricted to $\mathcal{B}_{\mathbf{\Delta}} = \{\Delta \in \mathbf{\Delta} : \forall i,\ \delta_i \in [-1, 1]\}$. In that case, the $(M(s), \Delta)$ interconnection is stable for all uncertainties $\Delta \in \mathcal{B}_{\mathbf{\Delta}}$ if and only if:

$$\sup_{\omega \in \mathbb{R}_+} \mu_{\mathbf{\Delta}}\left(M_{11}(j\omega)\right) \leq 1 \tag{23}$$

where $\mu_{\mathbf{\Delta}}(M_{11}(j\omega))$ is the structured singular value (SSV), introduced in [26]. Computation of the SSV is in general NP-hard, so that in practice, upper and lower bounds are computed instead.

The GSS library of the SMAC toolbox [27] is used to obtain an LFR of the closed-loop roll channel at the design point λ_{R0}. The resulting interconnection consists of a nominal system $M_R(s, \lambda_{R0})$ with 13 states and an uncertainty block Δ_R belonging to the set:

$$\mathcal{B}_{\mathbf{\Delta}R} = \left\{ \text{diag}\left(\delta_{C_A}, \delta_{C_{l\beta}}, \delta_{K_v}\right) : \delta_\bullet \in [-1, 1] \right\} \tag{24}$$

A μ-upper bound of $0.19 < 1$ is obtained with the SMART library of the SMAC toolbox [28], thus validating robust stability at the design point. The same analysis conducted at other flight points indicate that virtually identical robustness properties are guaranteed across the whole flight envelope.

Complementing the above analysis, Fig. 8 shows the responses for 300 random samples of the uncertain system at the design point, drawn uniformly from $\mathcal{B}_{\mathbf{\Delta}R}$, and for a scenario involving a step input of 45 deg at 0 s, and a step disturbance $d_o = 20$ deg applied at 1.5 s on ϕ_f. The responses are nearly identical, illustrating that the uncertainties on the roll channel have minimal impact. The disturbance is successfully rejected in all cases, and the control signal remains small in amplitude, and far from the saturation level of ± 10 deg. Similar simulations can be conducted on other points of the flight envelope, leading to dismissing the risk of saturations for the roll channel despite the variations of the coefficient $b_2(\lambda_R)$.

3.2 Pitch/yaw autopilot design

3.2.1 Control objectives and strategy

Autopilot design for the pitch/yaw channels is based on the bank of LTI models generated from the reduced flight envelope $\lambda_{PY} = [V\ h\ p_a]^{\mathrm{T}}$ (see Eq. (17)). The closed-loop settling time must be sufficiently large compared to the settling time of the roll channel (0.43 s), since the pitch/yaw autopilot is designed with the assumption that the roll angle is already settled, but small enough to ensure good

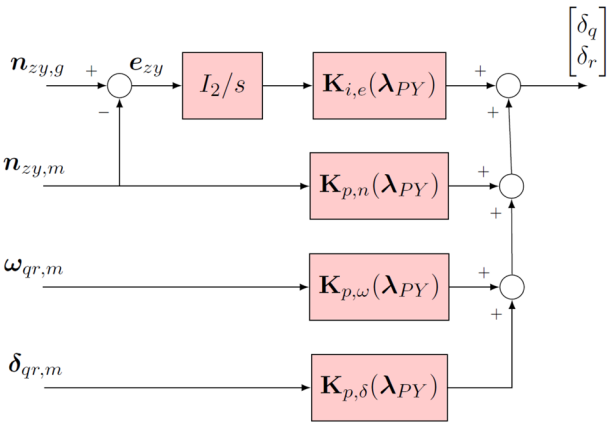

Fig. 9 Pitch/yaw autopilot structure

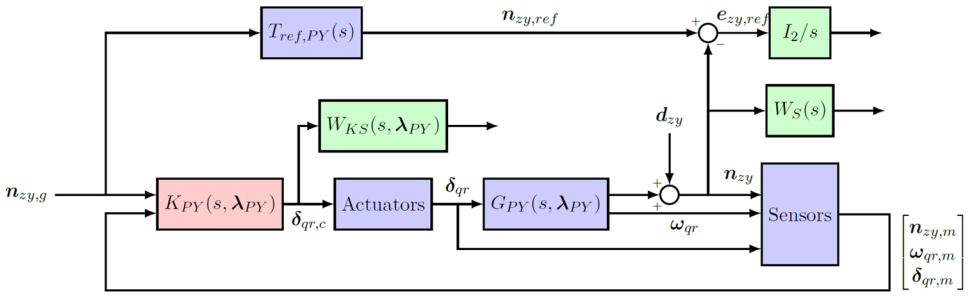

Fig. 10 Structured $\mathcal{H}_2/\mathcal{H}_\infty$ synthesis problem for the pitch/yaw autopilot

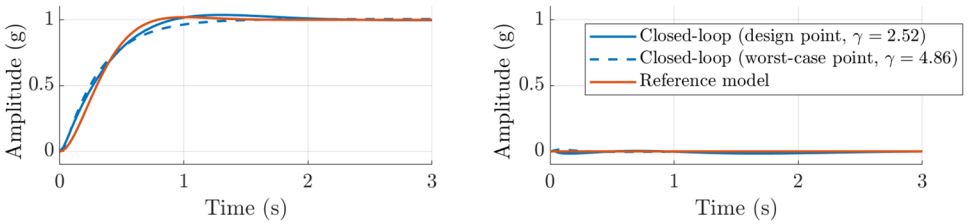

Fig. 11 Step response from $n_{z,g}$ to n_z (left) and from $n_{y,g}$ to n_z (right)

tracking of the guidance signal and, ultimately, good accuracy upon impact. Due to the strong coupling between the pitch and yaw axes, a multivariable control problem must be tackled. A low-order structured controller composed of few gains is preferred, so that linear interpolation can be used for gain-scheduling.

Remark 2 To lighten notations, the subscript ϵ representing deviation from equilibrium values is omitted in this section.

3.2.2 Autopilot structure and tuning

The proposed fixed-structure controller is presented in Fig. 9. Symmetries of the airframe model are exploited by imposing corresponding symmetries on the gain matrices of the controller, further reducing the interpolation and implementation effort:

$$\mathbf{K}_{i,e} = \begin{bmatrix} K_{i,e}^{(11)} & K_{i,e}^{(12)} \\ K_{i,e}^{(12)} & -K_{i,e}^{(11)} \end{bmatrix} \quad \mathbf{K}_{p,n} = \begin{bmatrix} K_{p,n}^{(11)} & K_{p,n}^{(12)} \\ K_{p,n}^{(12)} & -K_{p,n}^{(11)} \end{bmatrix}$$
$$\mathbf{K}_{p,\omega} = \begin{bmatrix} K_{p,\omega}^{(11)} & K_{p,\omega}^{(12)} \\ -K_{p,\omega}^{(12)} & K_{p,\omega}^{(11)} \end{bmatrix} \quad \mathbf{K}_{p,\delta} = \begin{bmatrix} K_{p,\delta}^{(11)} & K_{p,\delta}^{(12)} \\ K_{p,\delta}^{(12)} & -K_{p,\delta}^{(11)} \end{bmatrix} \tag{25}$$

The eight controller gains are computed by solving a mixed $\mathcal{H}_2/\mathcal{H}_\infty$ controller synthesis problem using `systune`. As with roll autopilot synthesis, weighting functions $W_S(s)$ and $W_{KS}(s)$ are defined to capture, respectively, disturbance rejection and control attenuation requirements, and a second-order system is used as a reference model for the system response, with frequency $\omega_{ref,PY} = 5$ rad/s and damping ratio $\xi_{ref,PY} = 0.781$. The associated soft goal is specified as a time-domain step tracking goal in `systune`[1]. With respect to the signals defined in Fig. 10, the quantity to minimize relates to the energy of the step response of the transfer function:

$$\mathcal{T}_{\boldsymbol{n}_{zy,g}\to\boldsymbol{e}_{zy,ref}}(s) = T_{ref,PY}(s) - \mathcal{T}_{\boldsymbol{n}_{zy,g}\to\boldsymbol{n}_{zy}}(s) \tag{26}$$

The $\mathcal{H}_2$ norm, which corresponds to the energy of the impulse response of a system,[2] is used to express the objective function. More precisely, `systune` minimizes the following quantity:

$$f(\boldsymbol{\kappa}_{PY}) = \frac{\left\| \frac{1}{s}\mathcal{T}_{\boldsymbol{n}_{zy,g}\to\boldsymbol{e}_{zy,ref}}(s) \right\|_2}{\eta \left\| \frac{1}{s}[T_{ref,PY}(s) - I] \right\|_2} \tag{27}$$

where $\boldsymbol{\kappa}_{PY}$ are the free variables of the problem, i.e., the eight controller gains in this case, and η is a user-defined positive scalar value representing the desired maximum relative matching error (higher values of η decrease the performance index, loosening the requirement), and taken as 0.05 here. Thus, the synthesis problem for a design point $\boldsymbol{\lambda}_{PY}$ of the reduced flight envelope takes the form:

[1] Using a more standard $\mathcal{H}_\infty$ soft goal of the form $\|W_M(s)\mathcal{T}_{\boldsymbol{n}_{zy,g}\to\boldsymbol{e}_{zy,ref}}(s)\|_\infty$, as with the roll channel, led to less robust margins, as well as less smooth gain surfaces when performing the synthesis over the flight envelope.

[2] Thus, the $\mathcal{H}_2$ norm of $G(s)/s$ corresponds to the energy of the step response of $G(s)$.

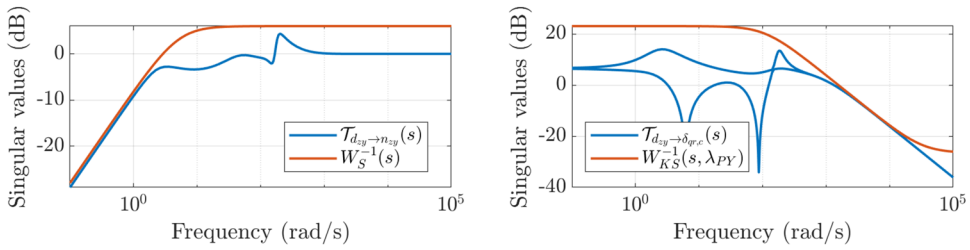

Fig. 12 Closed-loop transfer functions for disturbance rejection (left) and control attenuation (right)

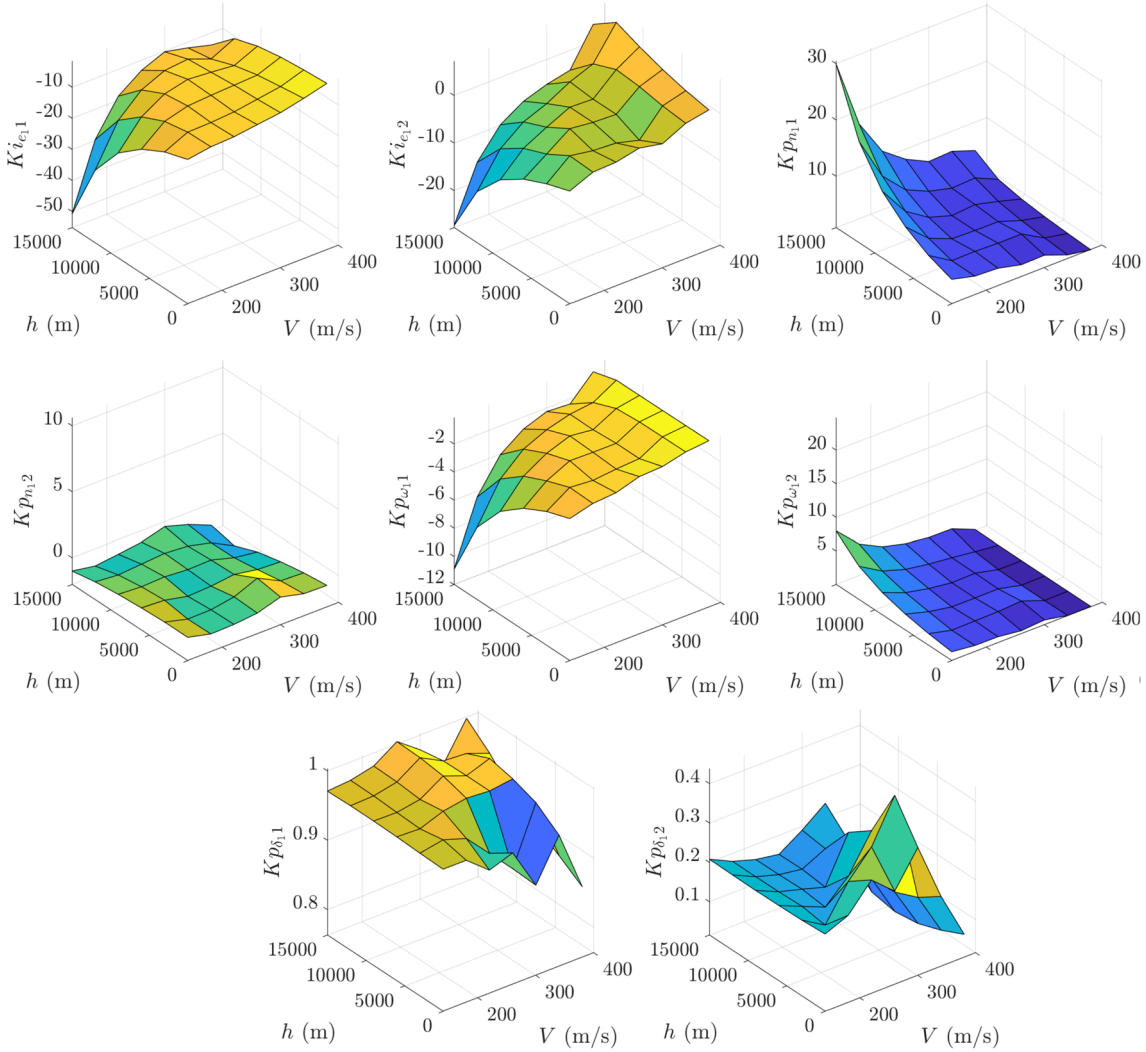

Fig. 13 Gain surfaces at $p_a = 750$ rad/s

$$\begin{aligned} \underset{\boldsymbol{\kappa}_{PY}}{\text{minimise}}\ & f(\boldsymbol{\kappa}_{PY}) \\ \text{subject to}\ & \|W_S(s)\mathcal{T}_{d_z\to n_z}(s)\|_\infty < 1 \\ & \|W_S(s)\mathcal{T}_{d_y\to n_y}(s)\|_\infty < 1 \\ & \|W_{KS}(s,\boldsymbol{\lambda}_{PY})\mathcal{T}_{\boldsymbol{d}_{zy}\to\boldsymbol{\delta}_{qr}}(s)\|_\infty < 1 \end{aligned} \tag{28}$$

The variations of the control authority across the flight envelope is taken into account through an appropriate parametrization of $W_{KS}(s, \boldsymbol{\lambda}_{PY})$. This is done by introducing a scaling factor $k(\boldsymbol{\lambda}_{PY})$, taken as the DC gain from the input δ_q to the output n_z. The weighting function $W_{KS}(s, \boldsymbol{\lambda}_{PY})$ is then parametrized as:

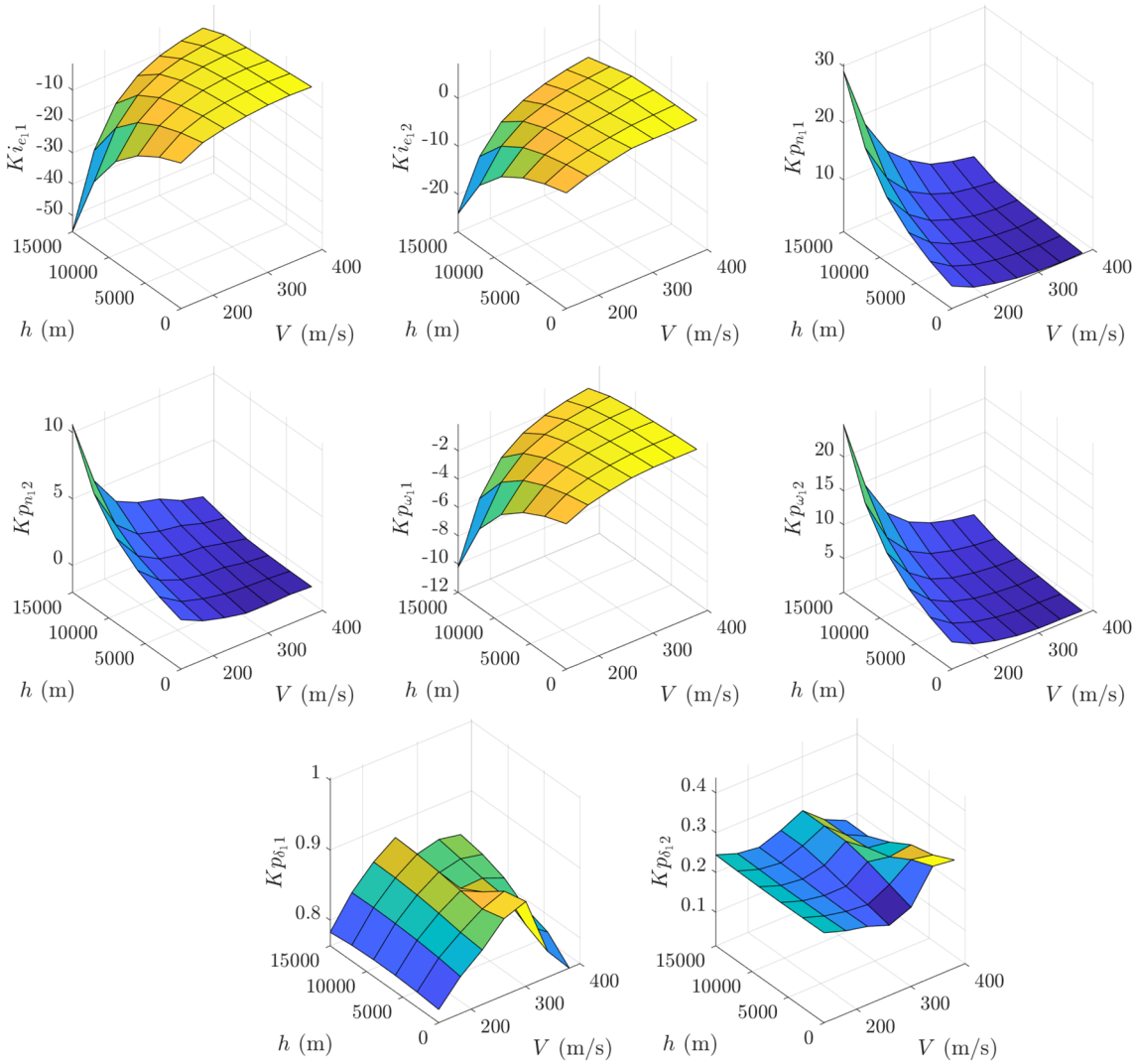

Fig. 14 Gain surfaces at $p_a = 1650$ rad/s

$$W_{KS}(s, \lambda_{PY}) = k(\lambda_{PY}) \cdot \hat{W}_{KS}(s) \tag{29}$$

with $\hat{W}_{KS}(s)$ to be tuned.

A design point λ_{PY0} corresponding to high velocity $V = 340$ m/s, low altitude $h = 0$ m, and intermediate spin rate $p_a = 1200$ rad/s is then selected to perform a first synthesis. This point corresponds to the end of a trajectory, where performance is critical to guarantee good terminal accuracy. The weighting functions are tuned as follows:

$$W_S(s) = \frac{s+5}{2s+5\times 10^{-4}} \qquad \hat{W}_{KS}(s) = \frac{s+110}{10^{-2}s+110\times 3} \tag{30}$$

The resulting closed-loop step response is shown in Fig. 11 for the normal axis, and corresponds to a soft goal value of 2.52. The signal n_z is satisfyingly close to the reference model response both in terms of guidance tracking (left plot) and cross-axis decoupling (right plot). Identical performances are achieved on the lateral axis (transfers from $\boldsymbol{n}_{zy,g}$ to n_y). Figure 12 shows the shaped transfer functions and illustrates the satisfaction of the hard constraints defined by the weighting functions. The same synthesis problem is solved on a $7 \times 6 \times 5$ grid of the reduced flight envelope (210 points). The hard constraints are satisfied for all design points, while the worst-case value of the soft goal reaches 4.86 at point $(V, h, p_a) = (380$ m/s, 9000 m, 750 rad/s). Nonetheless, the corresponding step response, also shown in Fig. 11, remains satisfactory. Figure 13 and 14 show the values of the controller gains, displayed as surfaces in (V, h) for the extremal values of p_a. The surfaces remain relatively smooth, with the notable exception of the gains $K_{p,\delta}^{(11)}$ and

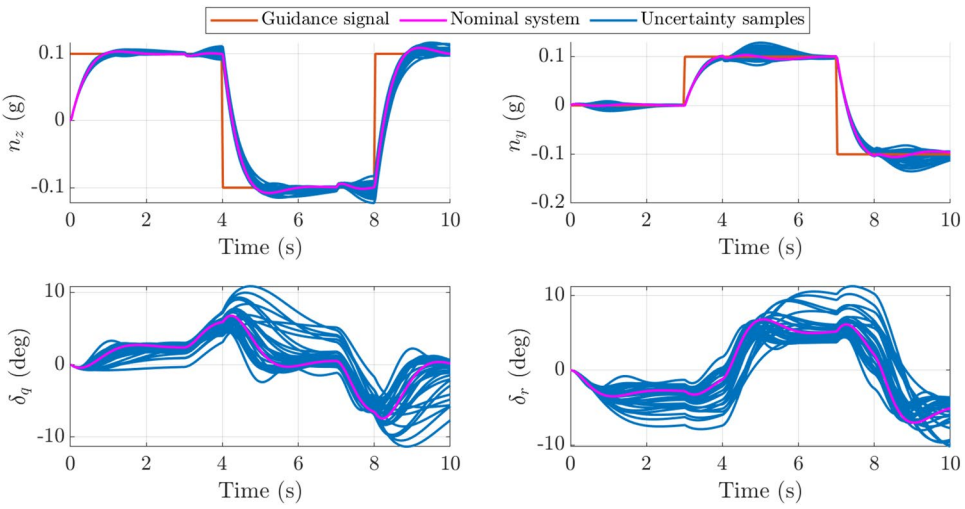

Fig. 15 Simulation with model uncertainties at the design point

$K_{p,\delta}^{(12)}$. However, this issue is mitigated by the fact that variations of these two gains are in fact restricted to a small interval.

3.2.3 Robustness analysis and time-domain simulations

Similar to the roll channel, a μ-analysis is used to verify local robust stability for all design points. The LFR models for the closed-loop pitch/yaw channels are parametrized by $\lambda_{PY} = \left[V\ h\ p_a\right]^{\mathrm{T}}$, and consist of a nominal system $M_{PY}(s, \lambda_{PY})$ with 16 states, and a 16×16 uncertainty block Δ_{PY} with associated unit ball:

$$\begin{aligned}\mathcal{B}_{\mathbf{\Delta}PY} = \Big\{ &\operatorname{diag}\left(\delta_{C_{N\alpha}} I_2, \delta_{C_{N\delta}} I_2, \delta_{C_A} I_2, \delta_{C_{Y p\alpha}} I_2,\right. \\ &\left.\delta_{C_{m\alpha}} I_2, \delta_{C_{mq}} I_2, \delta_{C_{m\delta}} I_2, \delta_{C_{np\alpha}} I_2\right) : \delta_\bullet \in [-1, 1]\Big\}\end{aligned} \tag{31}$$

Only one design point fails to validate robust stability, with a SSV located in the interval $[1.009,\ 1.02]$, for parameter values $V = 300$ m/s, $h = 3000$ m, and $p_a = 750$ rad/s. Interestingly, the value of the airspeed at this point is a bit below Mach 1, which corresponds to either extrema or strong variations of several aerodynamic coefficients. This is combined with a low value of p_a, for which gyroscopic stability is weaker, thus giving a physical interpretation of why robust stability is not achieved at this point. However, this analysis is conservative, since it does not take into account the probability distribution of the uncertainties. Using the branch-and-bound probabilistic μ-analysis developed in [29] shows that the probability of instability at this point is in fact very low, with an upper bound at 0.013% assuming a uniform distribution of the uncertainties. This probability lowers to approximately $9 \cdot 10^{-7}$% when considering truncated normal distributions where, for each uncertainty, the standard deviation σ is chosen so that 3σ corresponds to the maximum uncertainty level as reported in Table 1.

The impact of the uncertainties is visualized in the time-domain simulations of Fig. 15, which shows the responses of the nominal system and uncertain samples at the design point λ_{PY0}. Tracking and decoupling are moderately degraded, and more importantly, larger control signals are required by the autopilot. This hints at potential saturations with the proposed controller, justifying the need to develop an anti-windup compensator for the pitch/yaw axes.

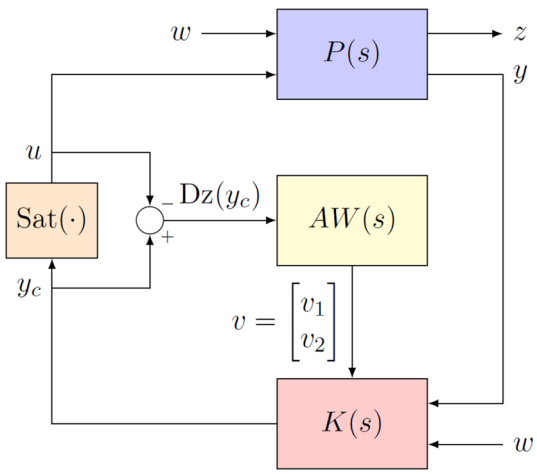

Fig. 16 Principle of anti-windup compensation

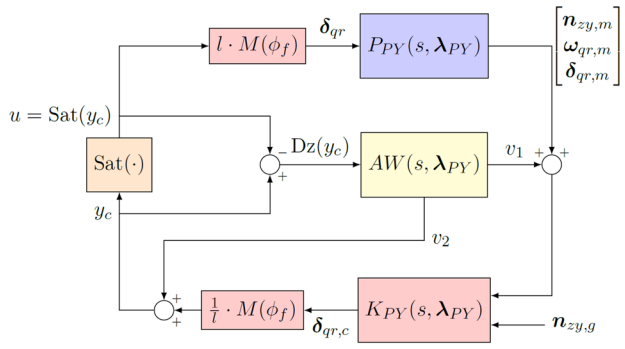

Fig. 17 Closed-loop system with anti-windup compensation

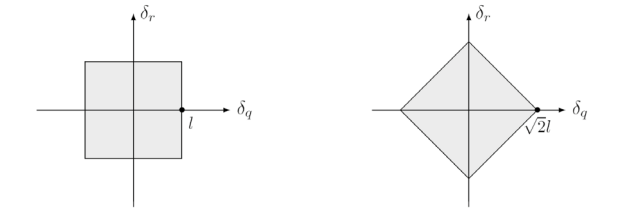

(a) '+' configuration: $\phi_f = 0\,\mathrm{deg}$ (b) '×' configuration: $\phi_f = 45\,\mathrm{deg}$

Fig. 18 Set of virtual control signals leading to no saturation

4 Anti-windup design

4.1 Anti-windup problem setup and synthesis method selection

The principle of anti-windup compensation in a time-invariant framework is illustrated by Fig. 16. The anti-windup compensator $AW(s)$ is driven by the difference $\mathrm{Dz}\,(y_c) = y_c - \mathrm{Sat}\,(y_c)$ between the desired controller output y_c and the achieved command $u = \mathrm{Sat}\,(y_c)$, and generates a signal $v = [v_1\ v_2]^{\mathrm{T}}$ that modifies the control dynamics.

In the studied application, the output signals of the baseline autopilot $\boldsymbol{\delta}_{qr,c} = [\delta_{q,c}\ \delta_{r,c}]^{\mathrm{T}}$ correspond to commanded virtual deflection angles, and are not adapted to design the anti-windup compensator, since the saturation level $l = 10\,\mathrm{deg}$ affects the commanded real deflection angles $\boldsymbol{\delta}_{R,c} = [\delta_{1,c}\ \delta_{2,c}\ \delta_{3,c}\ \delta_{4,c}]^{\mathrm{T}}$ instead. To fit into the anti-windup framework, the allocation is explicitly taken into account, with the assumption that the roll angle ϕ_f of the fuse is fixed at the desired position and that the contribution of the virtual control signal of the roll channel δ_p on the real deflection angles is negligible. The allocation is then given by:

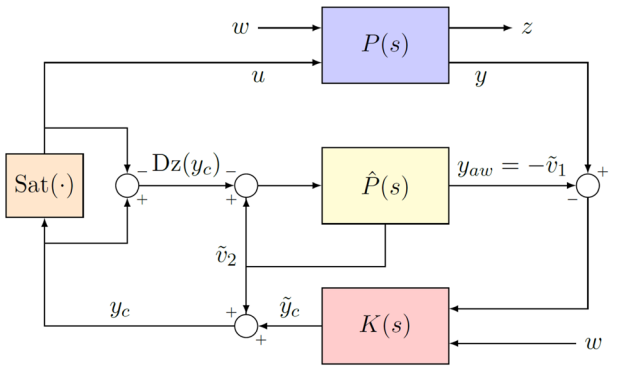

Fig. 19 MRAW architecture

$$\boldsymbol{\delta}_{R,c} = \begin{bmatrix} -\sin\phi_f & \cos\phi_f \\ \cos\phi_f & \sin\phi_f \\ \sin\phi_f & -\cos\phi_f \\ -\cos\phi_f & -\sin\phi_f \end{bmatrix} \boldsymbol{\delta}_{qr,c} \tag{32}$$

Eq. (32) implies $\delta_{1,c} = -\delta_{3,c}$ and $\delta_{2,c} = -\delta_{4,c}$. For the purpose of anti-windup synthesis, this makes the signals $\delta_{1,c}$ and $\delta_{3,c}$ redundant, as well as the signals $\delta_{2,c}$ and $\delta_{4,c}$. Thus, with reference to the standard anti-windup architecture of Fig. 16, we define the input y_c of the normalized saturation as:

$$y_c = \frac{1}{l}\begin{bmatrix}\delta_{1,c}\\ \delta_{2,c}\end{bmatrix} = \frac{1}{l}\begin{bmatrix}-\sin\phi_f & \cos\phi_f\\ \cos\phi_f & \sin\phi_f\end{bmatrix}\boldsymbol{\delta}_{qr,c} = \frac{1}{l}M(\phi_f)\boldsymbol{\delta}_{qr,c} \tag{33}$$

which is illustrated in Fig. 17 (note that $M^{-1}(\phi_f) = M(\phi_f)$), where $P_{PY}(s, \lambda_{PY})$ gathers the airframe (4 states), two virtual actuators ($2 \times 2 = 4$ states), and first-order sensors (two accelerometers, two gyroscopes, two servo-sensors: 6 states), leading to a plant of order 14.

Remark 3 The real actuator and servo-sensor models could be used in the plant model $P_{PY}(s, \lambda_{PY})$, increasing the plant order to 20. However, this does not modify the signals seen by the anti-windup compensator, and thus has no impact on the synthesis.

It is clear from Eq. (33) and the relation $u = \mathrm{Sat}\,(y_c)$ that the fuse roll angle ϕ_f contributes to determining whether saturations occur or not. In fact, for a fixed value of ϕ_f, the set of virtual signals (δ_q, δ_r) that will not lead to saturations can be represented as a square in the (δ_q, δ_r)-plane, whose orientation depends on ϕ_f. Figure 18 shows this set for the two standard fuse orientations, which are the '+' ($\phi_f = 0\,\mathrm{deg}$) and '×' ($\phi_f = 45\,\mathrm{deg}$) configurations. It can be observed that the '×' configuration allows to reach higher values of the virtual control signals. In terms of the overall projectile trajectory, and focusing on δ_r, this corresponds as a first approximation to a higher control authority on the

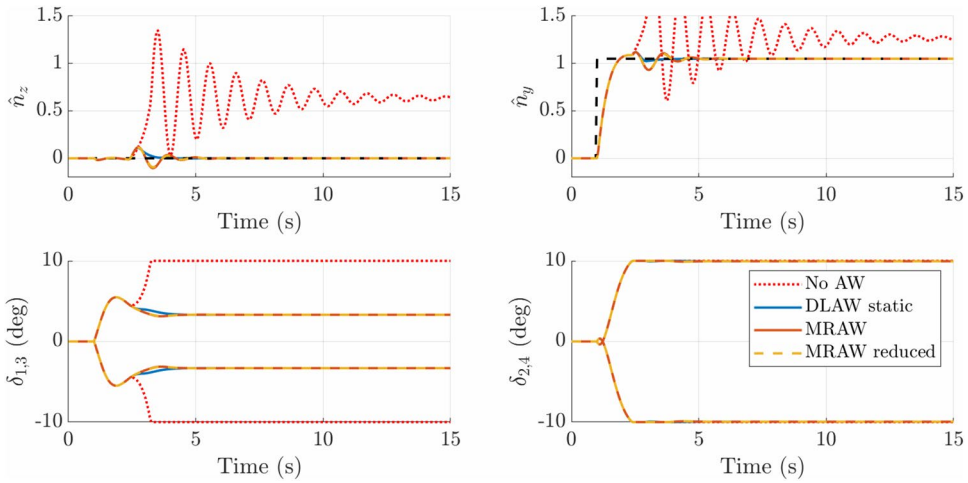

Fig. 20 Step responses for different anti-windup schemes

downrange error compared to the '+' configuration. This happens because, for $\phi_f = 45$ deg, all four canards contribute to generate the virtual signal δ_r, as opposed to only two canards in the case where $\phi_f = 0$ deg. The same interpretation also holds for δ_q and crossrange error. The drawback is a loss of versatility compared to the '+' configuration, in the sense that commanding $\delta_r \neq 0$ decreases the interval of compatible values of δ_q. Nevertheless, from nonlinear simulations of realistic launch scenarios without saturations (see Sect. 5), the '×' configuration seems preferable to limit the occurrence of saturations. Thus, the value $\phi_f = 45$ deg is used to synthesize the pitch/yaw anti-windup compensator.

A large panel of methods are available to compute anti-windup compensators in a time-invariant framework. Modern anti-windup theory, as described for instance in [19], identifies two families of methods: Direct Linear Anti-Windup (DLAW), and Model Recovery Anti-Windup (MRAW). The DLAW approach relies on Lyapunov stability theory and the modified sector condition from [30] to express the anti-windup design problem as a Linear Matrix Inequality (LMI) problem. The MRAW approach embeds a model $\hat{P}(s)$ of the plant in the anti-windup compensator, as illustrated by Fig. 19. This architecture allows to track the mismatch with respect to the unconstrained model through the state x_{aw} of the anti-windup compensator. The anti-windup signal $\tilde{v}_2$ then aims to minimize this mismatch. A notable feature of MRAW compensators is that they do not depend on the controller dynamics (i.e., on the baseline autopilot for the studied application). A drawback of this approach is that they are, by construction, of the order of the plant, which can be high, and therefore leads to a more complicated on-board implementation.

The DLAW and MRAW approaches are formulated in a time-invariant framework, and the theoretical guarantees regarding stability domains and performance levels are not preserved when varying parameters are involved. Nonetheless, they remain appealing to compute local compensators, to be subsequently interpolated using a gain-scheduling technique. In this context, it makes sense to favor methods requiring little or no tuning, as they are easier to implement over the whole flight envelope. Based on these considerations, three anti-windup methods are considered for local syntheses, which are done over the same $7 \times 6 \times 5$ grid of the reduced flight envelope (210 points) used for pitch/yaw autopilot synthesis.

The first method is a static DLAW synthesis method, with furthermore $v_2 = 0$ to avoid algebraic loops. The local syntheses are performed using the SAW library of the SMAC toolbox (https://w3.onera.fr/smac/saw) so as to maximize the amplitude of step input reference signals $\boldsymbol{n}_{zy,g}$ for which stability can be guaranteed [31]. The global compensator is then obtained by linearly interpolating the coefficients of the matrix $D_{aw,1} \in \mathbb{R}^{2\times 2}$. This design was first proposed in [32].

The second anti-windup compensator uses the LQ-based MRAW method applicable to unstable plants [19]. Thus, with respect to the block-diagram of Fig. 19, the anti-windup signal $\tilde{v}_2$ is computed as $\tilde{v}_2 = K_{lqr} x_{aw}$ so as to minimize the LQ performance index:

$$J = \int_0^\infty \left(x_{aw}^{\mathrm{T}} Q x_{aw} + \tilde{v}_2^{\mathrm{T}} R \tilde{v}_2 \right) \mathrm{d}t \tag{34}$$

The cost function is kept the same for all the design points, enforcing a stronger penalty on the four states corresponding to the (mismatch on the) actuator states with $Q = \mathrm{diag}\,(I_{10}, 50 \cdot I_4)$ and $R = I_2$. The relatively high order $n_{aw} = 14$ of the local compensators does not lend itself to the interpolation of state-space coefficients. Instead, the interpolation method chosen to obtain the global compensator is based on output blending [33]. This design was first proposed in [34].

To address the drawback of having plant-order MRAW compensators, a third anti-windup design is explored.

It consists of an LQ-based MRAW based on a reduced plant model, where the actuator and sensor dynamics are neglected and only the airframe dynamics remain. Thus, the resulting reduced MRAW compensator has order $n_{aw} = 4$. The computation is done using $Q = I_4$ and $R = I_2$, and output blending is used as the interpolation method.

It is worth noting that computation of the local LQ-based MRAW compensators is very fast, with the synthesis over all points of the flight envelope grid taking a bit over 6 s, both for the full and reduced cases. By contrast, synthesis of the 210 static DLAW compensators takes about 180 s. The relative length of the latter computation can be attributed to the required LMI resolution, although it should be pointed out that the SAW library uses LMI Lab as an LMI solver, and that CPU time reduction may be achieved using faster solvers such as SeDuMi [35] or MOSEK [36].

Figure 20 shows the closed-loop responses for different compensation schemes at the design point λ_{PY0}. The step amplitude of the reference signal $n_{y,g}$ is chosen as $n_{y,g} = 1.05 \cdot n_{y,sat}$, where $n_{y,sat}$ is the lowest value leading to real deflection angles above 10 deg within 10 s. The load factors shown in the figures are normalized as $\hat{n}_z = n_z/n_{y,sat}$ and $\hat{n}_y = n_y/n_{y,sat}$. Without anti-windup compensation, the deflection angles eventually all saturate, resulting in large errors on the load factors as well as badly damped oscillations. The anti-windup schemes all greatly improve the response, with the MRAW compensators featuring some additional small oscillations compared to the DLAW response. Remarkably, both the MRAW and reduced MRAW responses are identical, despite the significant order difference.

4.2 IQC analysis

4.2.1 Brief reminders on the IQC framework

The robustness of the closed-loop for fixed values of the scheduling variables is investigated using IQC analysis. This framework relies on an LFR representation of the system to analyze, and was introduced in [20], where the following main stability theorem is stated:

Theorem 1 *With respect to the interconnection of Fig. 7, let $M_{11}(s)$ be a stable LTI system and $\Delta \in \mathbf{\Delta}$ a bounded causal operator. Let $\Pi : j\mathbb{R} \to \mathbb{C}^{(n_{y_\Delta}+n_{u_\Delta})\times(n_{y_\Delta}+n_{u_\Delta})}$ a measurable Hermitian-valued function. Assume that*:

- *well-posedness is guaranteed for every $\tau \in [0, 1]$*, i.e. *$I - \tau M_{11}(s)\Delta$ has a causal inverse*;
- *for every $\tau \in [0, 1]$, $\tau\Delta$ satisfies the IQC defined by the multiplier* Π, i.e.:

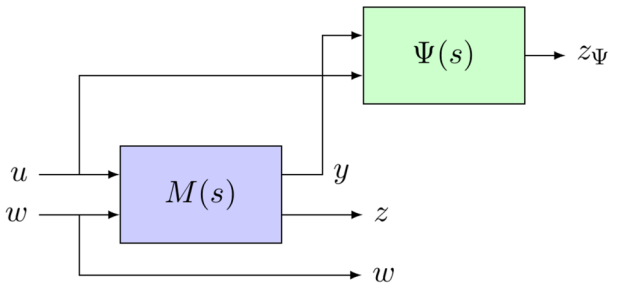

Fig. 21 IQC performance analysis

$$\forall y_\Delta \in \mathcal{L}_2 \int_{-\infty}^{+\infty} \begin{bmatrix} \hat{y}_\Delta(j\omega) \\ \hat{u}_\Delta(j\omega) \end{bmatrix}^* \Pi(j\omega) \begin{bmatrix} \hat{y}_\Delta(j\omega) \\ \hat{u}_\Delta(j\omega) \end{bmatrix} d\omega \geq 0 \tag{35}$$

with $u_\Delta = \tau\Delta(y_\Delta)$, and where $\mathcal{L}_2$ is the space of signals with finite energy, and for $f \in \mathcal{L}_2$, $\hat{f}$ denotes the Fourier transform of f;

- *there exists $\varepsilon > 0$ such that*:

$$\forall \omega \in \mathbb{R} \begin{bmatrix} M_{11}(j\omega) \\ I \end{bmatrix}^* \Pi(j\omega) \begin{bmatrix} M_{11}(j\omega) \\ I \end{bmatrix} \leq -\varepsilon I \tag{36}$$

Then the interconnection $(M_{11}(s), \Delta)$ is stable.

The strength of the IQC framework lies in the capacity to address simultaneous uncertainties of different nature, for instance parametric uncertainties and deadzone nonlinearities. Indeed, consider an operator $\Delta = \text{diag}\,(\Delta_1, \ldots, \Delta_N)$, where each individual block Δ_i satisfies the IQC defined by a multiplier Π_i. Then Δ satisfies the IQC defined by the composite multiplier Π given as:

$$\Pi = \begin{bmatrix} \text{diag}\left(\Pi_{1,11}, \ldots, \Pi_{N,11}\right) & \text{diag}\left(\Pi_{1,12}, \ldots, \Pi_{N,12}\right) \\ \text{diag}\left(\Pi_{1,12}^*, \ldots, \Pi_{N,12}^*\right) & \text{diag}\left(\Pi_{1,22}, \ldots, \Pi_{N,22}\right) \end{bmatrix} \tag{37}$$

where each Π_i is partitioned as $\Pi_i = \begin{bmatrix} \Pi_{i,11} & \Pi_{i,12} \\ \Pi_{i,12}^* & \Pi_{i,22} \end{bmatrix}$ according to the dimension of the corresponding Δ_i.

The numerous works on IQC theory provide multipliers for a wide variety of uncertainties and nonlinearities. As emphasized in [37], it is particularly convenient to work with multipliers parametrized as $\Pi = \Psi^* P \Psi$ with some fixed $\Psi \in \mathcal{RH}_\infty^{n_\Psi \times (n_y + n_u)}$ and $P = P^{\mathrm{T}} \in \boldsymbol{P} \subset \mathbb{R}^{n_\Psi \times n_\Psi}$, where $\boldsymbol{P}$ is described by LMI constraints capturing features of the uncertainty block. Indeed, application of the Kalman–Yakubovich–Popov (KYP) lemma then allows to replace the frequency-domain inequalities (36) by the equivalent condition:

Table 2 Computational burden of IQC analysis with deadzone nonlinearities and aerodynamic uncertainties

Configuration	No AW	Static DLAW	MRAW	Reduced MRAW
Order of the augmented system (minimal realization)	60	60	70	69
Number of decision variables	2012	2012	2667	2597
Average computation time (s)	11.7	9.9	17.2	17.1

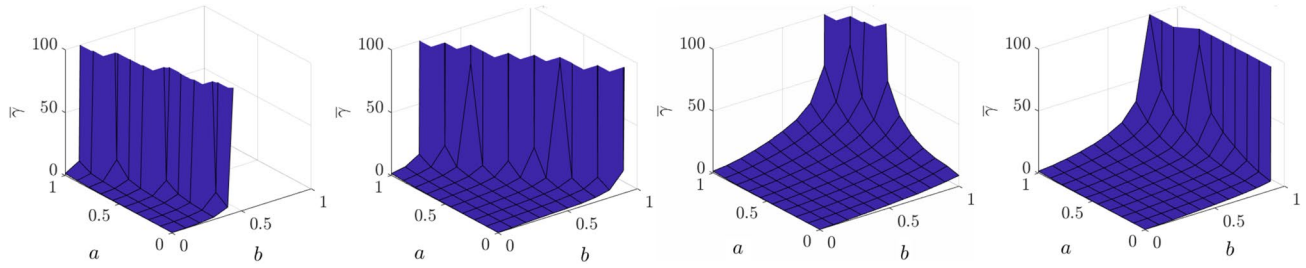

Fig. 22 Bounds on the $\mathcal{L}_2$-gain in the presence of aerodynamic uncertainties $|\delta_\bullet| \leq a$ and nonlinearity $\Phi \in \text{sec}[0,b]^2 \cap \textit{slope}[0,b]^2$; from left to right: no anti-windup, static DLAW, MRAW, reduced MRAW

- *there exists* $X = X^{\mathrm{T}}$ *of suitable dimension and* $P \in \boldsymbol{P}$ *such that:*

$$\begin{bmatrix} I & 0 \\ A & B \\ C & D \end{bmatrix}^{\mathrm{T}} \begin{bmatrix} 0 & X & 0 \\ X & 0 & 0 \\ 0 & 0 & P \end{bmatrix} \begin{bmatrix} I & 0 \\ A & B \\ C & D \end{bmatrix} < 0 \tag{38}$$

where (A, B, C, D) *is a minimal realization of the system* $\Psi(s) \begin{bmatrix} M_{11}(s) \\ I \end{bmatrix}$.

Thus, verifying stability of the interconnection boils down to solving an LMI problem.

The IQC framework extends seamlessly to performance analysis, by taking into account the performance channel from w to z. In particular, when evaluating performance through the $\mathcal{L}_2$ gain, the LMI (38) is adapted into:

$$\begin{bmatrix} I & 0 \\ \mathcal{A} & \mathcal{B} \\ \mathcal{C} & \mathcal{D} \end{bmatrix}^{\mathrm{T}} \begin{bmatrix} 0 & X & 0 \\ X & 0 & 0 \\ 0 & 0 & \mathcal{P} \end{bmatrix} \begin{bmatrix} I & 0 \\ \mathcal{A} & \mathcal{B} \\ \mathcal{C} & \mathcal{D} \end{bmatrix} < 0 \tag{39}$$

where $\mathcal{P} = \text{diag}\,(P, I_{n_z}, -\gamma^2 I_{n_w})$, and $(\mathcal{A}, \mathcal{B}, \mathcal{C}, \mathcal{D})$ is a minimal realization of the system in Fig. 21, from input $[u\ w]^{\mathrm{T}}$ to output $[z_\Psi\ z\ w]^{\mathrm{T}}$. We then seek matrices $X = X^{\mathrm{T}}$ and $\mathcal{P}$ that minimize γ under the LMI constraints (39) and $P \in \boldsymbol{P}$. This guarantees that the interconnection is robustly stable and provides an upper bound on the worst-case $\mathcal{L}_2$ gain from w to z.

Finally, from an implementation point of view, the IQC-analysis procedure based on the KYP lemma can be summarized as follows:

1. Build the interconnection $(M(s), \Delta)$, with $M(s)$ a stable LTI system, and where $\Delta = \text{diag}\,(\Delta_1, \ldots, \Delta_N)$ may contain different types of uncertainties and nonlinearities,
2. Select a valid class of multipliers $\Pi_i = \Psi_i^* P_i \Psi_i$ for each uncertainty Δ_i, where the Ψ_i are fixed (several choices are possible for a same class of multiplier), and each P_i belongs to a set $\boldsymbol{P}_i$ described by LMI constraints,
3. Build the composite multiplier $\Psi^* P \Psi$ based on Eq. (37),
4. Compute a minimal realization of the system of Fig. 21,
5. Minimize γ under the LMI constraints (39) and $P \in \boldsymbol{P}$.

4.2.2 Application to the guided projectile

To apply IQC analysis to the guided projectile, LFR models of the closed-loop pitch/yaw channels are first computed for the different anti-windup configurations using the GSS library. The resulting Δ block gathers both the 16×16 aerodynamic uncertainty block $\Delta_{PY} \in \mathcal{B}_{\boldsymbol{\Delta}_{PY}}$ as defined in Sect. 3, and a two-dimensional deadzone nonlinearity, leading to the augmented structure:

$$\hat{\mathcal{B}}_{\boldsymbol{\Delta}_{PY}} = \Big\{ \text{diag}\,\Big(\delta_{C_{N\alpha}} I_2, \delta_{C_{N\delta}} I_2, \delta_{C_A} I_2, \delta_{C_{Y p\alpha}} I_2, \delta_{C_{m\alpha}} I_2, \delta_{C_{mq}} I_2, \delta_{C_{m\delta}} I_2, \delta_{C_{np\alpha}} I_2, \text{Dz}\,(\cdot)\Big) : \delta_\bullet \in [-1, 1] \Big\} \tag{40}$$

The performance channel considered is taken as the transfer from the guidance signals $\boldsymbol{n}_{zy,g}$ to the error signals $\boldsymbol{e}_{zy,ref}$ with respect to the second-order reference model $T_{ref,PY}(s)$ (see Fig. 10).

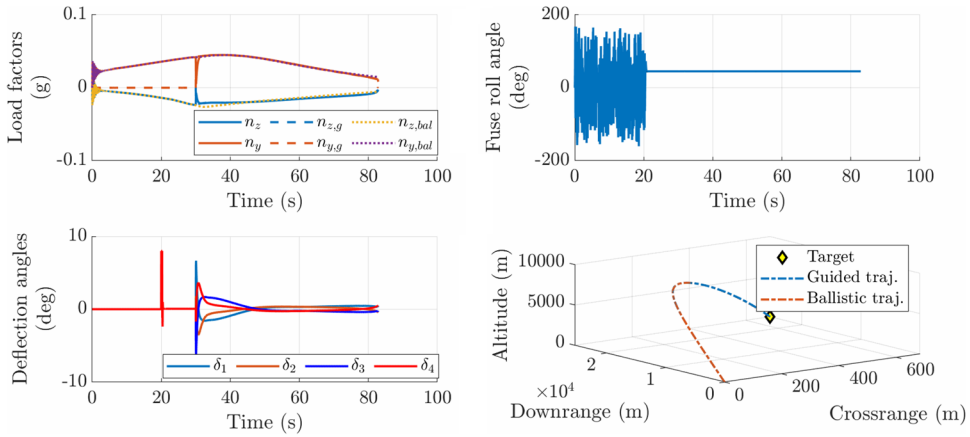

Fig. 23 Nominal scenario with baseline autopilot (no anti-windup)

A robustness analysis can then be done, including both the deadzone nonlinearities and aerodynamic uncertainties. The former are locally described as a sector bounded and slope-restricted nonlinearity $\Phi \in \text{sec}[0, b]^2 \cap \text{slope}[0, b]^2$. Accordingly, we use a combination of full-block circle criterion (see e.g. Class 13 in [37]) and full-block Zames–Falb multipliers [38]. The parametrization of the Zames–Falb multipliers requires the selection of real poles and their multiplicity to specify basis functions. Based on a few trials, two poles are chosen, -10 and -100, both with multiplicity 1. The latter are described using dynamic *DG*-scaling multiplier, with a pole -10 of multiplicity 1 for each uncertainty (see Class 5 in [37]). The normalized aerodynamic uncertainties are then allowed to vary between $[-a, a]$, with $a \leq 1$. This allows to compute upper bounds $\overline{\gamma}$ on the $\mathcal{L}_2$-gain of the uncertain system for given values of $b \in [0, 1]$ and $a \in [0, 1]$. Taking $a = 0$ corresponds to the IQC test with no aerodynamic uncertainties. Meanwhile, taking $b = 0$ corresponds to computing upper bounds on the worst-case $\mathcal{H}_\infty$ performance which can also be obtained using skew-μ analysis. Table 2 displays the LMI problem data corresponding to the IQC test and the average resolution time for given values of a and b.

Figure 22 depicts the surfaces obtained for the different anti-windup schemes. For the configurations without anti-windup and with static DLAW, it can be observed that the value of b for which stability is guaranteed reduces significantly as a grows. Both MRAW configurations are comparatively more robust, as for fixed b, an increase in a still leads to finite $\mathcal{L}_2$ gains in most (but not all) cases, although the bounds on the $\mathcal{L}_2$ performance are noticeably degraded. It is also worth noting that the surfaces obtained for both the MRAW and reduced MRAW are virtually equal for small to intermediate values of b, indicating that for the corresponding set of sector nonlinearities, the MRAW and reduced MRAW have similar robust performance properties.

5 Nonlinear flight simulations

In this section, complete guided flight scenarios are simulated by combining the open-loop nonlinear 7-DoF model of the projectile with the roll and pitch/yaw autopilots and the anti-windup compensators. In this study, perfect navigation is assumed, providing values of the scheduling variables V_{Nav}, h_{Nav}, $p_{a,Nav}$. In addition, the measured fuse roll angle $\phi_{f,m}$ is used to specify the transformation $M(\phi_{f,m})$ rather than the expected value of 45 deg (cf. Figure 17), ensuring that activation of the anti-windup compensator is based on the current fuse roll angle, and avoiding potential chattering effects in case it oscillates around 45 deg.

5.1 Description and simulation of a nominal flight scenario

A flight scenario representative of a standard long-range mission is considered, characterized by the following launch conditions:

$$V_0 = 939 \text{ m/s}, \quad \theta_0 = 42 \text{ deg}, \quad \psi_0 = 0 \text{ deg} \tag{41}$$

The mission target is set as the ballistic impact point of the projectile, located approximately 25 km downrange and 700 m crossrange from the launch point. The position of the target is taken into account in the closed-loop through a guidance module implementing the zero-effort-miss (ZEM)

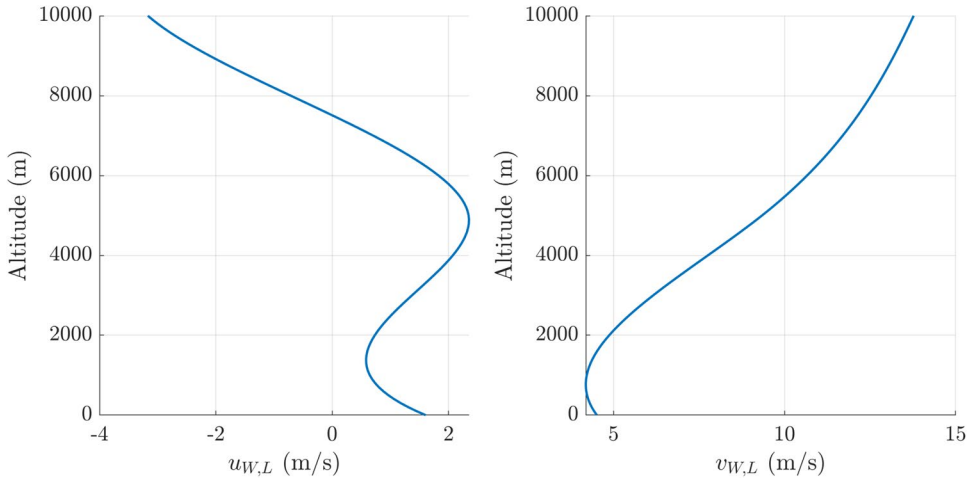

Fig. 24 Horizontal wind profile

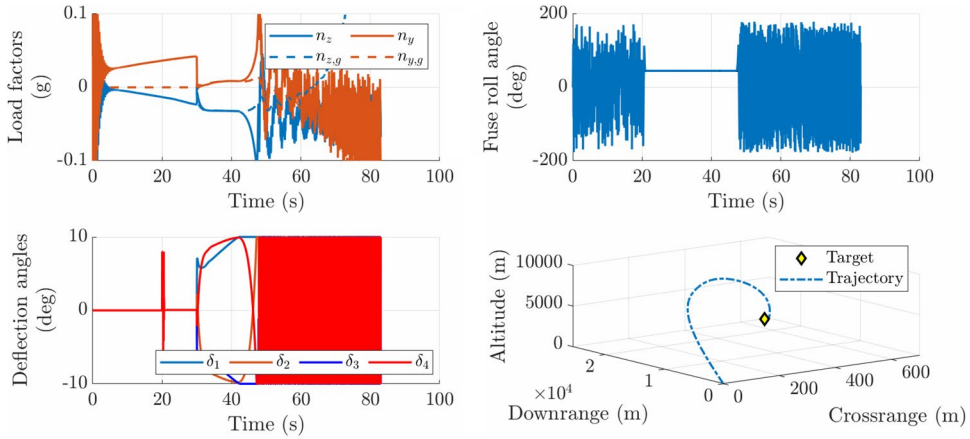

Fig. 25 Scenario with wind disturbance and resulting saturations

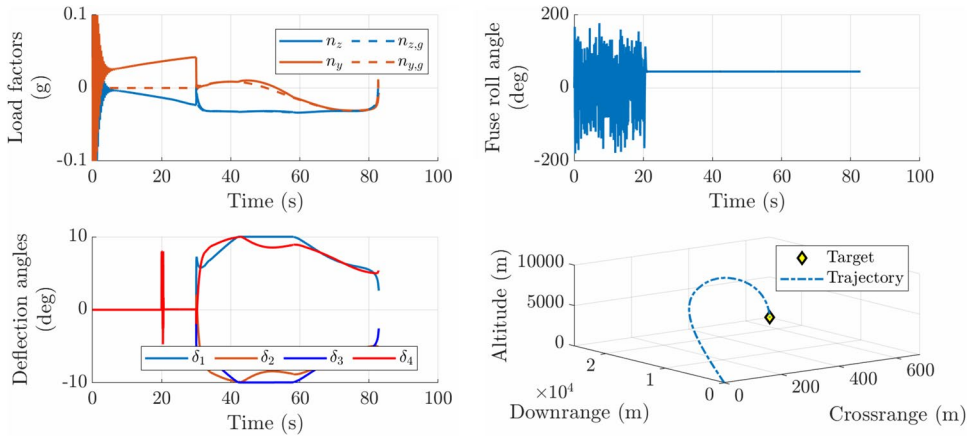

Fig. 26 Scenario with wind disturbance and scheduled static DLAW

guidance law developed in [39]. Briefly, ZEM guidance relies on an impact point prediction method to compute the lateral and longitudinal position errors between the target position and an estimated ballistic (zero-effort) impact point. These errors are regularly updated based on the current state of the projectile on a simplified model of the airframe, and serve as the basis to compute the guidance load factors $\boldsymbol{n}_{zy,g}$.

Simulation results with the baseline autopilot are shown in Fig. 23, where data from the ballistic trajectory are also provided for reference. Regarding the ballistic phase, it can be observed that the fuse configuration (p_f reduction and ϕ_f control) is very short, lasting about 0.5 s. Regarding the guided phase, the ZEM guidance law produces reference load factors $n_{z,g}$ and $n_{y,g}$ that are close to the ballistic ones

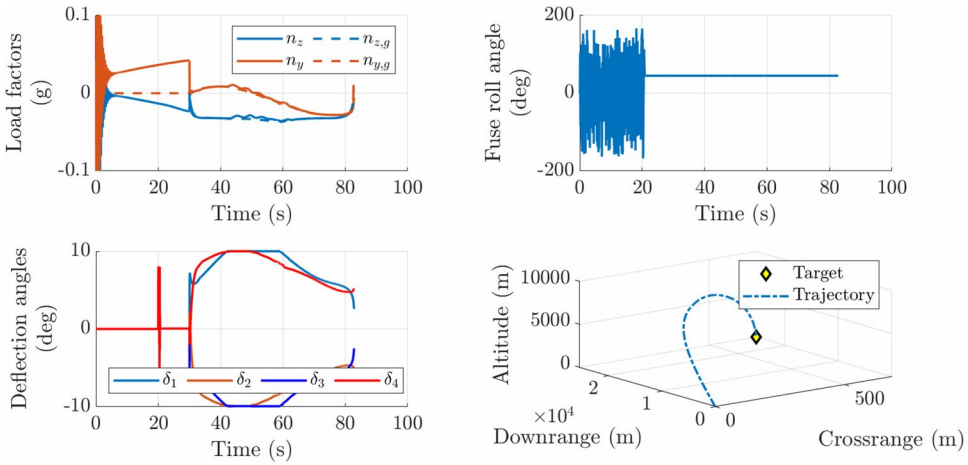

Fig. 27 Scenario with wind disturbance and scheduled reduced MRAW

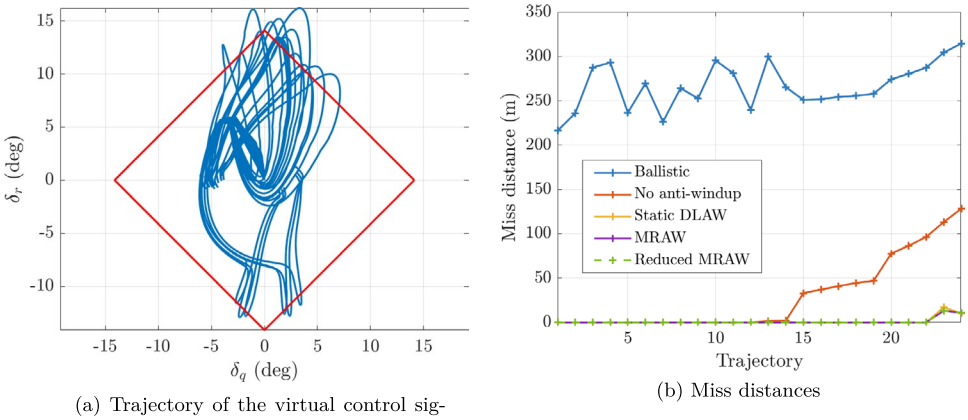

(a) Trajectory of the virtual control signals in the (δ_q, δ_r)-plane

(b) Miss distances

Fig. 28 Simulation results for the 24 launch uncertainty samples leading to deflection angles greater than $l = 10$ deg

Table 3 Global failure rate for maximum tolerated miss distance of 1, 10, and 20 m with uncertainties on launch conditions

Objective	No AW	With AW
< 1 m	2%	0.3%
< 10 m	1.7%	0.3%
< 20 m	1.7%	0%

$n_{z,bal}$ and $n_{y,bal}$. These guidance signals are tracked accurately by the pitch/yaw autopilot, leading to a miss distance at impact below one meter. Although the maximum tolerated miss distance may vary with the operational context, this order of magnitude corresponds unambiguously to a successful mission. Since the deflection angles remain below the saturation level $l = 10$ deg, identical trajectories are obtained regardless of the actuator model (linear or saturated) or anti-windup compensation used.

Remark 4 The 3D trajectories plotted in this section do not use equally scaled axes, since these are ill-suited to highlight the evolution along the y-axis (crossrange).

5.2 Simulations of degraded scenarios

The same mission with a horizontal wind disturbance is considered next. The coordinates of the wind velocity vector with respect to the Earth in the local-level frame are shown in Fig. 24. Since the cannon is oriented in the North direction ($\psi_0 = 0$ deg), the significant eastward component $v_{W,L}$ of the wind contributes to increase the deviation of the ballistic projectile to the right, leading to a miss distance of 427.1 m in the ballistic configuration. As seen on Fig. 25, deflection angles greater than 10 deg are required by the baseline autopilot. This leads to saturations, and ultimately mission failure in the absence of anti-windup compensation, with a miss distance of 67 m. Figures 26 and 27 then show results for the

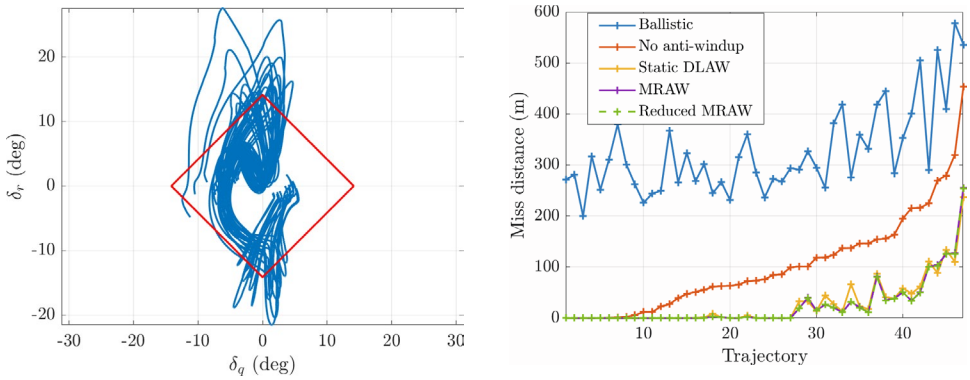

(a) Trajectory of the virtual control signals in the (δ_q, δ_r)-plane

(b) Miss distances

Fig. 29 Simulation results for the 47 aerodynamic uncertainty samples leading to deflection angles greater than $l = 10$ deg

Table 4 Global failure rate for maximum tolerated miss distances set to 1, 10, 20, and 50 m with aerodynamic uncertainties

Objective	No AW	DLAW	Full and reduced MRAW
< 1 m	13.7%	8%	7.7%
< 10 m	12.7%	6.7%	6.7%
< 20 m	12%	5.7%	5.3%
< 50 m	10.7%	3%	2.7%

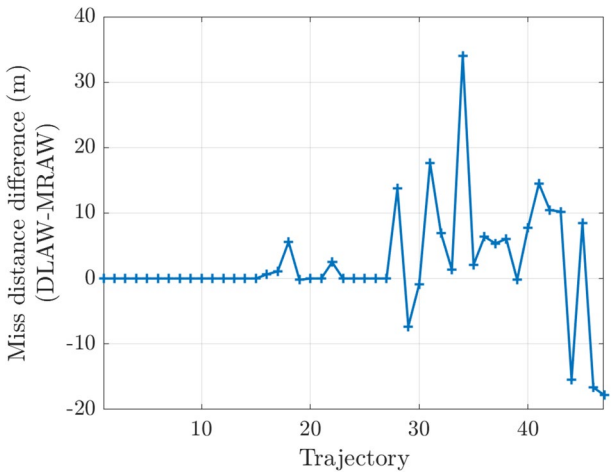

Fig. 30 Miss distance difference between DLAW and MRAW

same scenario, obtained with the scheduled static DLAW and reduced MRAW (the latter are nearly identical to those obtained with full MRAW). The guided projectile is able to recover a very satisfactory closed-loop behavior, with impact points located a mere 5 mm away from the mission target.

Remark 5 In practice, the wind vector is taken into account to define the initial yaw angle ψ_0 to bring the ballistic impact point closer to the target. This correction would contribute to reduce the deflection angles required by the autopilot, possibly to the point where anti-windup is not necessary. Nonetheless, the presented scenario with no adaptation of ψ_0 remains relevant to illustrate the increased maneuverability provided by anti-windup compensation.

Next, degraded scenarios involving uncertainties are considered. A first batch of 600 Monte Carlo trajectories with uncertainties on the initial launch conditions is generated. The samples are drawn following normal distributions, with mean values given by Eq. (41) and standard deviations 3 m/s, 0.09 deg, and 0.12 deg, respectively, for V_0, θ_0, and ψ_0. With no saturations, the miss distance at impact is less than a meter for all tested trajectories. However, 24 (4%) samples involve deflection angles exceeding $l = 10$ deg and reaching up to 14 deg. The left plot of Fig. 28 depicts the trajectory of the virtual control signals in the (δ_q, δ_r)-plane for these 24 samples. The interior of the red square represents the set of virtual control signals that do not lead to canard deflection angles greater than $l = 10$ deg in amplitude, assuming $\phi_{f,m} = 45$ deg and neglecting the contribution of δ_p in the allocation. This plot illustrates that the '×' configuration is better suited than the '+' configuration in limiting the excess of control from the pitch/yaw autopilot.

The right plot of Fig. 28 shows the miss distance corresponding to the 24 identified samples leading to saturations, for different projectile configurations: ballistic, with the baseline autopilot only (i.e., with no anti-windup), and with the 3 scheduled anti-windup compensators (static DLAW, MRAW, and reduced MRAW). The samples are sorted by increasing order of the miss distance for the baseline configuration. Some values are reported in Table 3, where no distinction between the different anti-windup compensators is made, since their performance is very similar.

The robustness of the nonlinear closed-loop to aerodynamic uncertainties is studied next. To this end, 300

Monte Carlo simulations are performed. The sampling of the aerodynamic coefficients is done assuming a normal distribution, where the standard deviation σ is such that 3σ corresponds to maximum uncertainty as reported in Table 1. Note that the aerodynamic uncertainties also impact the ZEM guidance, since it relies on nominal values of the aerodynamic coefficients. Nonetheless, the terminal accuracy of the guided projectile without saturations remains below one meter for all 300 simulations. However, 47 (15.7%) trajectories feature deflection angles exceeding $l = 10\,\text{deg}$, with 24 deg as a worst-case value. The trajectories of the virtual control signals for these samples are shown in the left plot of Fig. 29, where it is clear that aerodynamic uncertainties have more impact on the commanded deflection angles compared to launch uncertainties.

The miss distances for the 47 identified samples are shown in the right plot of Fig. 29 for the different projectile configurations. Table 4 shows the global failure rate with respect to a few values for the maximum accepted miss distance. Performance degradations with aerodynamic uncertainties on the baseline design are noticeably more severe compared to those stemming from launch uncertainties, with a noticeable loss of accuracy for almost all scenarios. The anti-windup compensators are able to mitigate this loss, although high miss distances are still reached in some cases. In addition, Fig. 30 shows the miss distance difference between DLAW and reduced MRAW compensation for the 47 samples. Samples associated to positive values then correspond to cases where MRAW compensation leads to a lower miss distance compared to DLAW compensation. Thus, the MRAW compensators seem to be slightly better in general at reducing the impact point dispersion, although this does not hold for every sample. Notably, Sample #47, associated to the greatest miss distance, performs worse with MRAW than with DLAW.

6 Conclusion

The objective of this paper is to design an autopilot for a novel guided dual-spin projectile concept steered by four independently actuated canards, subject to model uncertainties and actuator saturations. In a first step, gain-scheduled baseline autopilots, which do not take into account saturations, are developed for both the roll and the pitch/yaw channels using robust $\mathcal{H}_\infty$ control theory. The resulting closed-loop systems display very good local robustness properties, as evaluated with μ-analysis. Saturations are addressed in a second step through the addition of an anti-windup compensator to the closed-loop. Simple methods requiring little or no tuning are preferred for the synthesis of local compensators, to make computation over the whole flight envelope easier. Three such methods are selected, which are a static stability-based direct linear anti-windup (DLAW), an LQ-based model-recovery anti-windup (MRAW), and a reduced LQ-based MRAW. Local robustness analysis using integral quadratic constraints (IQC), taking into account both deadzone nonlinearities and aerodynamic uncertainties, confirms the improved robust stability properties of the augmented closed-loop systems. Coverage of the flight envelope is then ensured through linear interpolation of the gains for the static DLAW, and through output blending for the two MRAW schemes. Finally, the various closed-loop configurations are evaluated through operational flight scenarios involving a wind disturbance, perturbed launch conditions, or aerodynamic uncertainties. Simulation results demonstrate that the studied application can be successfully addressed using a combination of linear techniques and anti-windup compensation, with the proposed compensators improving the maneuverability of the system over the baseline autopilot.

Future work could investigate whether more sophisticated anti-windup techniques can further improve the current performance and robustness properties of the system. To this end, it could be interesting to decrease the conservatism of the IQC analysis by considering more representative profiles for the exogenous input signals. Another follow-up would be to integrate in the study a realistic navigation system, as well as sensor noise and computational delays. The increased complexity of the resulting system may demand further design iterations, and possibly some fine-tuning.

Acknowledgements This research is supported by the French-German Research Institute of Saint-Louis, and ONERA, the French Aerospace Lab.

Declarations

Conflicts of interest The authors have no relevant financial or non-financial interests to disclose.

References

1. Jitpraphai, T., Costello, M.: Dispersion reduction of a direct fire rocket using lateral pulse jets. J. Spacecr. Rockets **38**(6), 929–936 (2001). https://doi.org/10.2514/2.3765
2. Burchett, B., Peterson, A., Costello, M.: Prediction of swerving motion of a dual-spin projectile with lateral pulse jets in atmospheric flight. Math. Comput. Model. **35**(7–8), 821–834 (2002). https://doi.org/10.1016/S0895-7177(02)00053-5
3. Hahn, P.V., Frederick, R.A., Slegers, N.: Predictive guidance of a projectile for hit-to-kill interception. IEEE Trans. Control Syst. Technol. **17**(4), 745–755 (2009). https://doi.org/10.1109/tcst.2008.2004440
4. Frost, G., Costello, M.: Control authority of a projectile equipped with an internal unbalanced part. J. Dyn. Syst. Meas. Contr. **128**(4), 1005 (2006). https://doi.org/10.1115/1.2363205

5. Rogers, J., Costello, M.: A variable stability projectile using an internal moving mass. Proc. Inst. Mech. Eng. Part G J. Aerosp. Eng. **223**(7), 927–938 (2009). https://doi.org/10.1243/09544100jaero509
6. Cooper, G.R., Costello, M.: Trajectory prediction of spin-stabilized projectiles with a liquid payload. J. Spacecr. Rockets **48**(4), 664–670 (2011). https://doi.org/10.2514/1.52564
7. Theodoulis, S., Wernert, P.: Flight dynamics & control for smart munition: the ISL contribution. IFAC-PapersOnLine **50**(1), 15512–15517 (2017). https://doi.org/10.1016/j.ifacol.2017.08.2127
8. Fresconi, F.: Guidance and control of a projectile with reduced sensor and actuator requirements. J. Guid. Control. Dyn. **34**(6), 1757–1766 (2011). https://doi.org/10.2514/1.53584
9. Costello, M., Peterson, A.: Linear theory of a dual-spin projectile in atmospheric flight. J. Guid. Control. Dyn. **23**(5), 789–797 (2000). https://doi.org/10.2514/2.4639
10. Gagnon, E., Lauzon, M.: Maneuverability analysis of the conventional 155mm gunnery projectile. In: AIAA Guidance, Navigation and Control Conference and Exhibit, American Institute of Aeronautics and Astronautics, 2007. https://doi.org/10.2514/6.2007-6784
11. Gagnon, E., Lauzon, M.: Course correction fuze concept analysis for in-service 155 mm spin-stabilized gunnery projectiles. In: AIAA Guidance, Navigation and Control Conference and Exhibit, American Institute of Aeronautics and Astronautics, 2008. https://doi.org/10.2514/6.2008-6997
12. Theodoulis, S., Sève, F., Wernert, P.: Robust gain-scheduled autopilot design for spin-stabilized projectiles with a course-correction fuze. Aerosp. Sci. Technol. **42**, 477–489 (2015). https://doi.org/10.1016/j.ast.2014.12.027
13. Sève, F., Theodoulis, S., Wernert, P., Zasadzinski, M., Boutayeb, M.: Gain-scheduled H_∞ loop-shaping autopilot design for spin-stabilized canard-guided projectiles. AerospaceLab J. (2017). https://doi.org/10.12762/2017.AL13-03. (**ISSN: 2107-6596**)
14. Sève, F., Theodoulis, S., Wernert, P., Zasadzinski, M., Boutayeb, M.: Flight dynamics modeling of dual-spin guided projectiles. IEEE Trans. Aerosp. Electron. Syst. **53**(4), 1625–1641 (2017). https://doi.org/10.1109/taes.2017.2667820
15. Rugh, W.J., Shamma, J.S.: Research on gain scheduling. Automatica **36**(10), 1401–1425 (2000). https://doi.org/10.1016/s0005-1098(00)00058-3
16. Leith, D.J., Leithead, W.E.: Survey of gain-scheduling analysis and design. Int. J. Control **73**(11), 1001–1025 (2000). https://doi.org/10.1080/002071700411304
17. Skogestad, S., Postlethwaite, I.: Multivariable Feedback Control: Analysis and Design. Wiley-Interscience (2005)
18. Thai, S.: Advanced anti-windup flight control algorithms for fast time-varying aerospace systems. Ph.D. thesis, Toulouse, ISAE (2021)
19. Galeani, S., Tarbouriech, S., Turner, M., Zaccarian, L.: A tutorial on modern anti-windup design. Eur. J. Control. **15**(3–4), 418–440 (2009). https://doi.org/10.3166/ejc.15.418-440
20. Megretski, A., Rantzer, A.: System analysis via integral quadratic constraints. IEEE Trans. Autom. Control **42**(6), 819–830 (1997). https://doi.org/10.1109/9.587335
21. Zipfel, P.H.: Modeling and Simulation of Aerospace Vehicle Dynamics, 2nd edn. American Institute of Aeronautics and Astronautics (2007). https://doi.org/10.2514/4.862182
22. McCoy, R.L.: Modern Exterior Ballistics: The Launch and Flight Dynamics of Symmetric Projectiles. Schiffer Publishing (1999)
23. Siouris, G.M.: Missile Guidance and Control Systems. Springer (2004). https://doi.org/10.1007/b97614
24. Theodoulis, S., Gassmann, V., Brunner, T., Wernert, P: Fixed structure robust control design for the 155mm canard-guided projectile roll-channel autopilot. In: Proceedings of the 21st Mediterranean Conference on Control and Automation, IEEE, 2013. https://doi.org/10.1109/med.2013.6608714
25. Apkarian, P., Noll, D.: Nonsmooth H_∞ Synthesis. IEEE Trans. Autom. Control **51**(1), 71–86 (2006). https://doi.org/10.1109/tac.2005.860290
26. Doyle, J.: Analysis of feedback systems with structured uncertainties. IEE Proc. D Control Theory Appl. **129**(6), 242 (1982). https://doi.org/10.1049/ip-d.1982.0053
27. Biannic, J.M., Roos, C.: Generalized State Space: a new Matlab class to model uncertain and nonlinear systems as Linear Fractional Representations (2012-2021). http://w3.onera.fr/smac/gss. Accessed 25 Nov 2021
28. Roos, C.: Systems modeling, analysis and control (SMAC) toolbox: an insight into the robustness analysis library. In: Proceedings of the 2013 Conference on Computer Aided Control System Design (CACSD), IEEE, 2013. https://doi.org/10.1109/cacsd.2013.6663479
29. Thai, S., Roos, C., Biannic, J.M.: Probabilistic μ-analysis for stability and H∞ performance verification. In: Proceedings of the 2019 American Control Conference (ACC), IEEE, 2019. https://doi.org/10.23919/acc.2019.8814315
30. Gomes da Silva, J.M., Tarbouriech, S.: Antiwindup design with guaranteed regions of stability: an LMI-based approach. IEEE Trans. Autom. Control **50**(1), 106–111 (2005). https://doi.org/10.1109/tac.2004.841128
31. Biannic, J.M., Tarbouriech, S.: Optimization and implementation of dynamic anti-windup compensators with multiple saturations in flight control systems. Control. Eng. Pract. **17**(6), 703–713 (2009). https://doi.org/10.1016/j.conengprac.2008.11.002
32. Thai, S., Theodoulis, S., Roos, C., Biannic, J.M., Proff, M.: Gain-scheduled autopilot design with anti-windup compensator for a dual-spin canard-guided projectile. In: Proceedings of the 2020 IEEE Conference on Control Technology and Applications (CCTA), IEEE, 2020. https://doi.org/10.1109/ccta41146.2020.9206311
33. Kelly, J., Evers, J.: An interpolation strategy for scheduling dynamic compensators. Guidance, Navigation, and Control Conference. American Institute of Aeronautics and Astronautics (1997). https://doi.org/10.2514/6.1997-3764
34. Thai, S., Theodoulis, S., Roos, C., Biannic, J.M.: An interpolated model recovery anti-windup for a canard-guided projectile subject to uncertainties. In: Proceedings of the 2021 European Control Conference (ECC), IEEE, 2021. https://doi.org/10.23919/ECC54610.2021.9655059
35. Sturm, J.F.: Using SeDuMi 1.02, a MATLAB toolbox for optimization over symmetric cones. Optim. Methods Softw. **11**(1–4), 625–653 (1999)
36. MOSEK ApS, The MOSEK optimization toolbox for MATLAB manual. Version 9.0 (2019). http://docs.mosek.com/9.0/toolbox/index.html. Accessed 25 Nov 2021
37. Veenman, J., Scherer, C.W., Köroğlu, H.: Robust stability and performance analysis based on integral quadratic constraints. Eur. J. Control. **31**, 1–32 (2016). https://doi.org/10.1016/j.ejcon.2016.04.004
38. Fetzer, M., Scherer, C.W.: Full-block multipliers for repeated, slope-restricted scalar nonlinearities. Int. J. Robust Nonlinear Control **27**(17), 3376–3411 (2017). https://doi.org/10.1002/rnc.3751
39. Proff, M., Theodoulis, S.: Study of impact point prediction methods for zero-effort-miss guidance: application to a 155mm spin-stabilized guided projectile. In: Proceedings of the 5th CEAS Conference on Guidance, Navigation and Control (2019)